Paleoceanography and Paleoclimatology

RESEARCH ARTICLE
10.1029/2021PA004222

Special Section:
Cenozoic Evolution of Mountains, Monsoons, and the Biosphere

Evolution of Sea Surface Hydrology Along the Western Australian Margin Over the Past 450 kyr

Renjie Pei[1], Wolfgang Kuhnt[1], Ann Holbourn[1], Janika Jöhnck[1], Johanna Hingst[1,2], Sebastian Beil[1], Julia Lübbers[1], and Nils Andersen[3]

[1]Institute of Geosciences, Christian-Albrechts-University, Kiel, Germany, [2]MARUM—Center for Marine Environmental Sciences, University of Bremen, Bremen, Germany, [3]Laboratory for Radiometric Dating and Stable Isotope Research, Christian-Albrechts-University, Kiel, Germany

Key Points:

- Southwest front of modern Indo-Pacific Warm Pool (IPWP) during austral fall is located between 23° and 24°S
- Western Australian Margin north of 15°S remained seasonally influenced by IPWP throughout past 450 kyr
- Upper ocean hydrology off Western Australia represents an integrated signal of monsoonal precipitation and advective mixing

Supporting Information:

Supporting Information may be found in the online version of this article.

Correspondence to:

R. Pei,
renjie.pei@ifg.uni-kiel.de

Citation:

Pei, R., Kuhnt, W., Holbourn, A., Jöhnck, J., Hingst, J., Beil, S., et al. (2021). Evolution of sea surface hydrology along the Western Australian Margin over the past 450 kyr. *Paleoceanography and Paleoclimatology*, *36*, e2021PA004222. https://doi.org/10.1029/2021PA004222

Received 22 JAN 2021
Accepted 11 OCT 2021

Abstract We collected a suite of core top samples during R/V Sonne Cruise SO257 in May 2017 along the southwestern front of the Indo-Pacific Warm Pool (IPWP) to monitor the variability of Southern Hemisphere tropical and subtropical sea surface hydrology and to assess temperature and salinity reconstructions with data sets reflecting conditions in the post-monsoonal season. In our core top samples, a steep increase in planktic $\delta^{18}O$, associated with a decrease in sea surface temperature (SST), indicates that the southwestern front of the IPWP is located between 23° and 24°S during austral fall. We additionally reconstructed SST, sea surface salinity ,and $\delta^{18}O$ seawater ($\delta^{18}O_{sw}$) over the last 450 kyr in two sediment successions located within and beyond the monsoonal rain belt. Our records show that SST was highly coherent and phase-locked with atmospheric pCO_2 during the last 450 kyr. The regional differences in the $\delta^{18}O_{sw}$ records reveal that the Western Australian Margin north of 15°S remained seasonally under the influence of IPWP water masses, even during glacials. The temporal variability in upper ocean hydrology along the Western Australian Margin is not directly coupled to local monsoonal precipitation, but is strongly affected by advective mixing of Indonesian Throughflow derived water masses.

1. Introduction

The influence of precessional insolation and latitudinal insolation gradients on tropical hydrology, in particular the intensity and spatial extent of the Indonesian-Australian monsoonal rain belt, is still a matter of debate, since extended, orbital scale records remain extremely scarce (e.g., Holbourn et al., 2005; P. Zhang et al., 2020), as most studies focused on the last glacial cycle (e.g., Ayliffe et al., 2013; Denniston et al., 2013; Eroglu et al., 2016; Field et al., 2017; Ishiwa et al., 2019; Kuhnt et al., 2015; Mohtadi et al., 2011). Global sea surface temperature (SST) stacks over the last deglaciation indicated significant inter-hemispheric differences during deglacial warming, in particular for the phasing between globally increasing atmospheric carbon dioxide and regional warming in both hemispheres (Shakun et al., 2012). This global compilation included high-resolution SST reconstructions over the last two glacial terminations in the Timor Sea (Xu et al., 2008, 2006, 2010), at locations situated within the Indo-Pacific Warm Pool (IPWP). However, these reconstructions were based on Mg/Ca thermometry of near-surface and upper thermocline dwelling planktic foraminifers in an area directly influenced by the Indonesian Throughflow (ITF) and, thus, inherit some Northern Hemisphere temperature signature, such as a cool Heinrich Stadial 1 (HS1, ~15–18 ka) and an onset of deglacial warming during the Bølling/Allerød (~13–15 ka). Cores in the tropical Indian Ocean offshore southern Java, within the Timor Strait, Flores Sea, and Makassar Strait exhibit a similar delayed warming trend following HS 1 (Holbourn et al., 2011; Mohtadi et al., 2011; Schröder et al., 2018).

Substantial regional cooling in the Northern Hemisphere and widespread drying in the subtropics and tropics in the early stage of the last deglaciation (HS 1) were originally attributed to a southward shift of the Intertropical Convergence Zone (ITCZ) and associated tropical rain belt (Broccoli et al., 2006; Chiang & Bitz, 2005; Chiang et al., 2003; Chiang et al., 2008; Claussen et al., 2003; Muller et al., 2008, 2012). However, a global data compilation demonstrated that the height of this stadial (~16–17 ka) coincided with an extreme and widespread megadrought, which also affected the Southern Hemisphere (Stager et al., 2011). The widespread extent of the HS 1 megadrought suggests a severe weakening of the entire tropical convective rainfall system, probably as a response to tropical sea surface cooling on a global scale. Temperature, precipitation, and monsoonal sediment discharge proxy records from the subtropical Indian Ocean and off

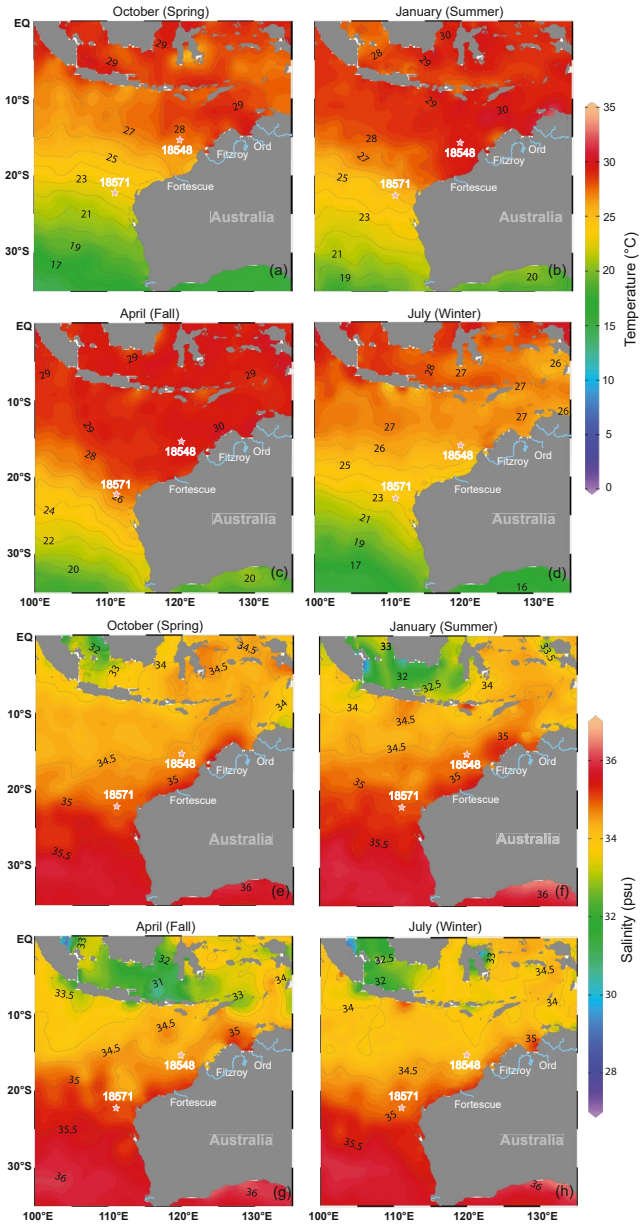

Figure 1. Seasonal distribution of modern sea surface (0 m) temperatures and salinities in the eastern Indian Ocean and along the Western Australian Margin. Data from WOA13 on 0.25° grids (Locarnini et al., 2013; Zweng et al., 2013) plotted using Ocean Data View (Schlitzer, 2021).

northwestern Australia indicated a major intensification of the Australian monsoon at ~13 ka (De Deckker et al., 2014; Denniston et al., 2013; Field et al., 2017; Ishiwa et al., 2019; Kuhnt et al., 2015). However, the occurrence of widespread tropical aridification reaching into the Southern Hemisphere during the early stage of deglaciation, when atmospheric pCO_2 levels were still substantially lower than pre-industrial, remains uncertain. Insights into the phase relationships between precessional insolation, atmospheric pCO_2, local SST, and monsoonal discharge over several glacial terminations are, thus, critical for a better understanding of the processes driving climate warming and convective rainfall intensification in the Southern Hemisphere.

On orbital timescales, Northern and Southern Hemisphere temperature records exhibit an unexpected similar response to precessional insolation forcing with temperature maxima at precession minima (Northern Hemisphere insolation maxima; Huybers & Denton, 2008; Laepple et al., 2011; Uemura et al., 2018). Southern Hemisphere monsoonal proxy records display a similar response to insolation/temperature forcing with maxima in monsoonal intensity close to precession minima even though Southern Hemisphere peak daily summer insolation was at a minimum (e.g., P. Zhang et al., 2020). Several mechanisms have been suggested to explain this phase-locked behavior of climate on the precessional band in the two hemispheres: (a) extended austral summer duration (maximum number of days with high average insolation in the Southern Hemisphere) at precession minima (Huybers, 2009); (b) maximum daily insolation in austral spring (September) at precession minima, which decreases sea ice cover around Antarctica and intensifies heat transfer toward the Antarctic interior with repercussions over the entire Southern Hemisphere (Timmermann et al., 2009); (c) zonal and cross-equatorial transfer of the Northern Hemispheric insolation signal to the Southern Hemisphere by atmospheric or ocean circulation (Chiang et al., 2008; Deininger et al., 2020); (d) steepening of latitudinal insolation gradients driven by the interference of precessional forcing and orbital obliquity (Bosmans et al., 2018; Chiang & Friedman, 2012; Mantsis et al., 2014).

Here, we monitor the variability of Southern Hemisphere tropical and subtropical hydrology in core top samples collected during R/V Sonne Cruise SO257 in May 2017 at sensitive locations along the southwestern front of the IPWP. We additionally reconstruct SST, sea surface salinity (SSS), and $\delta^{18}O$ seawater ($\delta^{18}O_{sw}$) over the last 450 kyr in two sediment successions located at the southwestern edge of the IPWP (within the monsoonal rain belt) and southwest of the IPWP (outwith the monsoonal rain belt). Our main objectives are to monitor the variability of Southern Hemisphere tropical and subtropical SST and SSS on millennial timescales and to relate their variability to sediment discharge records of the Australian monsoon, insolation forcing, high-latitude climate evolution, and changing atmospheric greenhouse gas concentrations.

2. Regional Oceanographic and Climatic Setting

The hydrologic setting at the southwestern margin of the IPWP is crucial for understanding climate evolution on the Australian continent and tropical climate interactions between the Pacific and Indian Oceans. The Western Australian Margin along the eastern Indian Ocean is characterized by a steep SST gradient from temperatures above 28°C within the IPWP to the northeast to cooler temperatures with stronger seasonal variability between 22°C and 25°C to the southwest (Figure 1). There is also a marked

northeastern-southwestern SSS gradient with higher salinities to the southwest (Figure 1). The seasonal variability of SST and SSS along the margin is affected by the intensity of the ITF and Leeuwin Current, which carry warm, low salinity water from the Timor Strait and eastern part of the North West Shelf toward the southwest (Church et al., 1989; Feng et al., 2015; Fieux et al., 2005). The seasonal salinity gradient is influenced both by the lower salinity of Banda and Arafura Sea waters that are transported by the ITF through the Timor Strait and along the North West Shelf and by freshwater discharge from the large rivers that drain the northern Australian monsoonal region (Phillips et al., 2005). The pathways and annual cycle of this important freshwater source were recently examined using oceanographic Lagrangian particle tracking modeling (Kida et al., 2019). This modeling study suggested that the dispersion of freshwater from the center of the Indonesian seas toward the eastern Indian Ocean is accompanied by evaporation, entrainment, and vertical mixing along the outflow pathway and takes an overall ~6 months. Thus, maximum austral summer monsoon rainfall that forms a major freshwater reservoir in the Java-Flores Sea in January–February reaches the Timor Strait outflow and the Northwest Cape in July–August (Figure 1). The temperature gradient along the coast offshore the Northwest Cape is additionally influenced by intermittent periods of strong equatorward winds during austral summer, which lead to lateral advection of cooler water masses from the southwest and periodically intensified wind-driven vertical mixing with subsurface waters (Taylor & Pearce, 1999; Woo et al., 2006). However, the seasonality of these equatorward countercurrents, which appear to weaken during fall and winter, remains an issue of debate (Lowe et al., 2012).

The seasonal dynamics of the IPWP southwestern front are strongly influenced by the interplay of the ITF and Leeuwin Current. The latter is initiated through a sea-level build-up by monsoonal winds during December–February in the Gulf of Carpentaria (Ridgway & Godfrey, 2015). The Leeuwin Current flows southward along the continental shelf of northwestern Australia as a shallow (<300 m), narrow band (<100 km wide) of warm, lower salinity, nutrient-depleted water of tropical origin, which mixes with cooler and saltier waters from the northward flowing West Australian Current during austral summer (Church et al., 1989; Cresswell & Peterson, 1993; Pattiaratchi, 2006; Ridgway & Condie, 2004; Smith et al., 1991). The unusually warm Leeuwin Current is seasonally strongest during austral fall and winter (May–July) and on an interannual time scale during La Nin~a years. Intensification of the Leeuwin Current promotes evaporative heat loss and upper ocean stratification and reduces upper ocean mixing, nutrient fluxes, and productivity (Feng et al., 2009). The current intensity is additionally increased by the heat flux over the Pilbara region during late austral summer, since increasing depth-averaged temperatures on the Pilbara shelf contribute to elevated sea level, when the warm surface water is vertically mixed by strong tides. This leads to seasonal advection of warm water westward and southward (Ridgway & Godfrey, 2015). The sea-level anomaly that drives the current system propagates southward against the prevailing wind direction and dominates the surface ocean along the Western Australia Margin during austral fall and early winter.

The seasonal discharge of the major northern (Alligator, Daly, Johnson, Pentecost, Victoria, Mary) and northwestern (Fitzroy, Ord) Australian rivers reach the coast at the end of the austral summer monsoon season (Figure 2). The total annual discharge of these larger rivers is relatively low (in the order of 56 km^3/yr, Milliman & Farnsworth, 2011), but highly seasonal with $\delta^{18}O$ values of precipitation in the range of −6‰ vs. VSMOV (Vienna Standard Mean Ocean Water) during the monsoonal season in the Darwin area (Liu et al., 2010). This discharge affects SSS and $\delta^{18}O$ mainly in the post-monsoonal season in the areas adjacent to the river mouths. However, the signal is intensified by direct precipitation into the sea, and contributes to a first salinity minimum along the Western Australian Margin in early austral fall (March–May; Figure 2). For the few rivers, where sediment load and discharge data are available (e.g., Ord River, Milliman & Farnsworth, 2011), the ratio of sediment to freshwater discharge is high, which is likely due to the high seasonality and lack of vegetation cover in the more elevated parts of the catchments.

3. Materials and Methods

3.1. Core Locations and Sediment Recovery

We analyzed a suite of surface sediment samples from core tops retrieved with a multicorer in May 2017 during R/V Sonne Cruise SO257 WACHEIO (Kuhnt et al., 2017). The 37 core top sediment samples were retrieved within the area of 15°3.591′S, 120°18.846′E and 27°15.325′S, 112°2.177′E along the Western Australian Margin (Figure 3, Table S1 in Supporting Information S1). This data set from the sediment-water

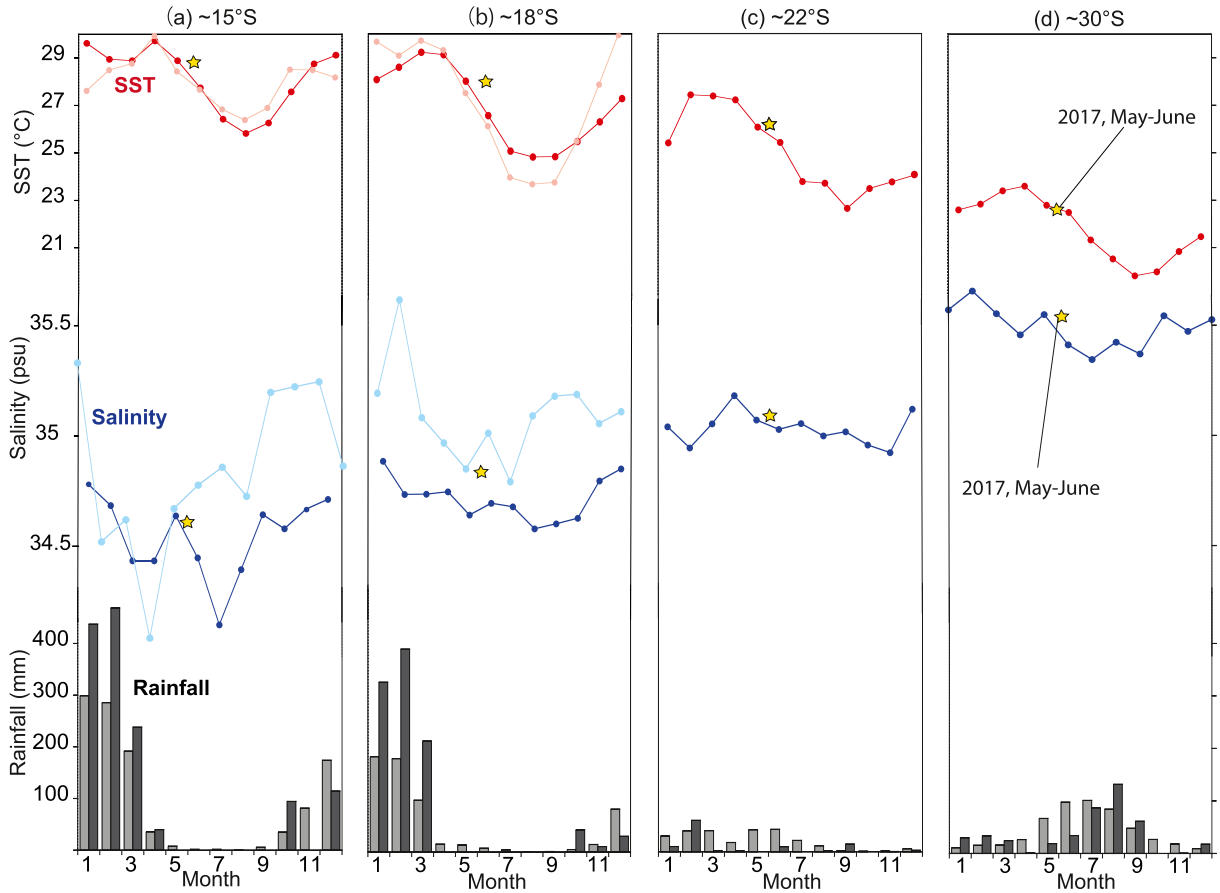

Figure 2. Monthly records of sea surface temperature (SST), salinity (WOA13), and rainfall (http://www.bom.gov.au/climate) along the Western Australian Margin. Red and blue curves indicate temperature and salinity at 0 m from WOA13: (a) 15.1°S/120.3°E; (b) 18.4°S, 115.2°E; (c) 22.1°S/113.5°E; (d) 29.0°S/112.9°E. Pink and light blue curves indicate temperature and salinity close to mouths of Ord River and Fitzroy River: (a) 15°S/124.6°E; (b) 18°S/121.9°E. Gray columns show mean precipitation from 1961 to 2020; black columns show precipitation in 2017: (a) Station Legune, 15.21°S/129.45°E; (b) Station Yeeda, 17.62°S/123.65°E; (c) Station Learmonth airport, 22.24°S/114.10°E; (d) Station Badgingarra, 30.34°S/115.54°E. Yellow stars indicate SST and SSS measured during R/V Sonne Cruise SO257 in May 2017.

interface is compared to downcore measurements in two sediment successions spanning the last four glacial-interglacial cycles that are located in contrasting oceanographic and climatic settings along the Western Australian Margin (Figure 3).

The composite sediment succession from piston Core SO257-18548 (15°3.591′S, 120°18.846′E, 1,608 m water depth, 11.2 m core length) and nearby International Ocean Discovery Program (IODP) Expedition 363 Site U1482 (15°3.32′S, 120°26.10′E, 1,466 m water depth) is located close to the modern southern limit of the seasonal (austral summer) displacement of the ITCZ (Figure 3b). The sediment records from Core SO257-18548 and Site U1482 were spliced into a composite record because a local sediment gravity flow eroded sediments younger than Marine Isotope Stage (MIS) 9 at Site U1482. The sediment from these locations consists of homogenous mottled olive greenish gray to dark gray clay-rich calcareous ooze (Kuhnt et al., 2017; Rosenthal et al., 2018).

Gravity Core SO257-18571 (22°6.666′S, 113°29.688′N, 1,052 m water depth, 20.1 m core length), retrieved in the southern part of the Exmouth Plateau, offshore the North West Cape Peninsula (Figure 3c), is situated south of the modern southern limit of the ITCZ. The sediment at this location consists of clay-rich nannoplankton ooze with distinct intercalations of dark reddish brown, clay-rich intervals, and light olive gray calcareous ooze (Kuhnt et al., 2017).

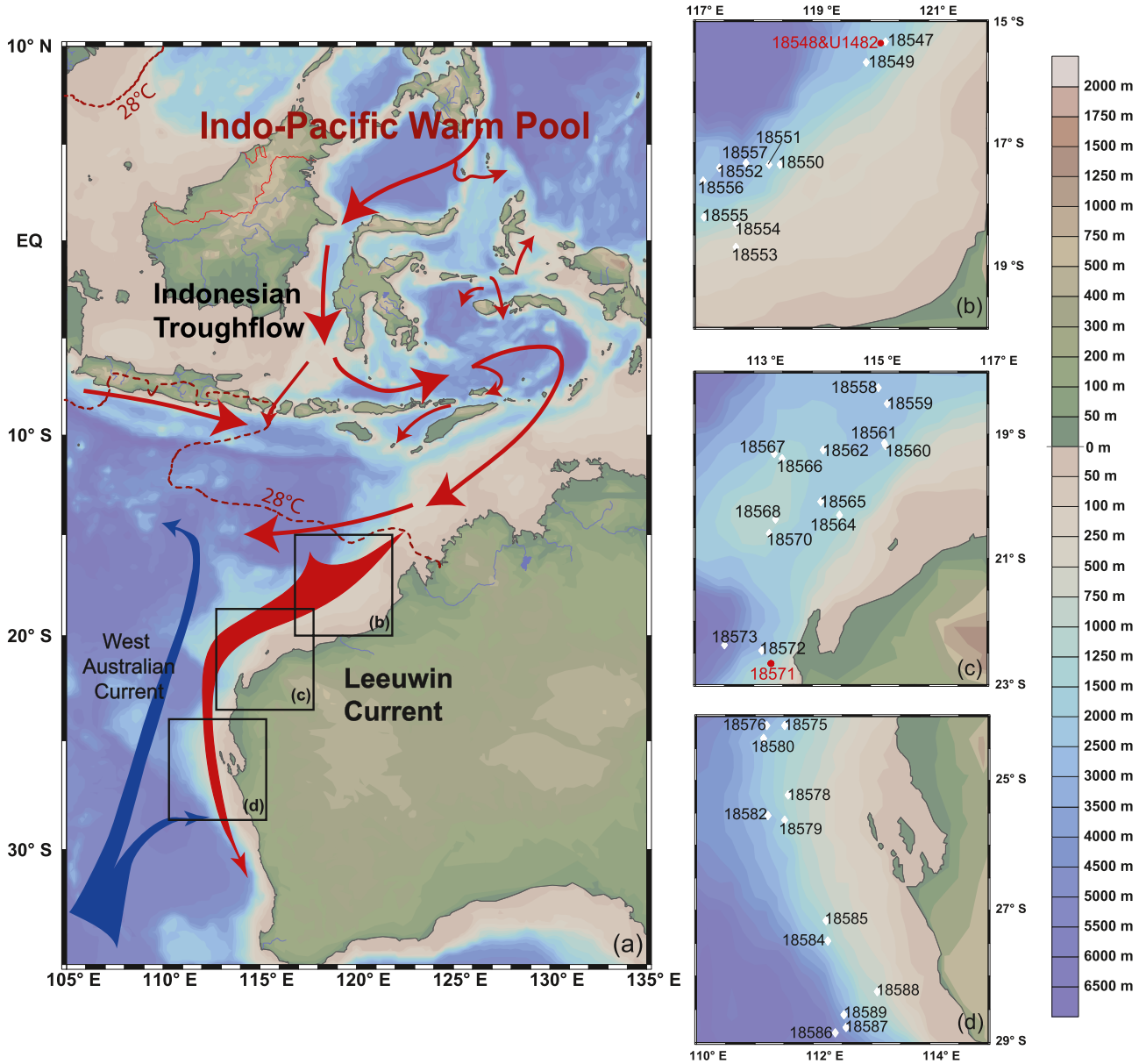

Figure 3. Oceanographic setting and core locations along the Western Australian Margin. (a) Major ocean circulation pathways. Red thin arrows: Indonesian Throughflow (Gordon et al., 2012), red thick arrow: Leeuwin Current, blue thick arrow: West Australian Current (Gallagher et al., 2009). Red dashed lines indicate the 28°C limit of annual SST from WOA13. (b– d) Locations cored during R/V Sonne Cruise SO257. Red dots indicate positions of Core SO257-18548, IODP Expedition 363 Site U1482, and Core SO257-18571. White dots indicate locations of core top samples analyzed in this study Map created with Ocean Data View (Schlitzer, 2021).

3.2. Sampling and Processing

We measured austral fall SST, SSS, and $\delta^{18}O_{sw}$ in the second half of May 2017 during R/V Sonne Cruise SO257 and compared these measurements to reconstructed SST, SSS, and $\delta^{18}O_{sw}$ from multi-corer core tops retrieved between the 1,000 and 2,000 m water isobaths. The year 2017 was an unusually wet and warm year in the monsoonal region of the Northern Territories and the northeastern part of Western Australia, while the west coast of Western Australia was drier than usual. Total annual rainfall across the Northern Territories was 19% above average mainly due to several wet months in the rainy season earlier in the year. Western Australian annual rainfall was 42% above average, mainly recorded in the monsoonal northern and eastern parts of Western Australia (http://www.bom.gov.au).

Multicores were sampled immediately after retrieval in 1 cm slices and the uppermost five slices were preserved in a mixture of ethanol and Rose Bengal in 300 ml Kautex bottles. An SBE 911 plus conductivity temperature depth (CTD) profiler was used at 10 stations to record the vertical variability of temperature, salinity, and oxygen, and to obtain water samples over the water profiles. The shipboard CTD of R/V Sonne is equipped with a rosette sampler with 24 Niskin bottles. $\delta^{18}O_{sw}$ was analyzed with a GasBench II, which is connected to a DeltaPlusXL mass spectrometer from the three uppermost Niskin bottles deployed at 5, 10, and 20 m below sea surface. Between stations, SST and SSS were continuously measured using a Seabird thermosalinograph mounted to the hull of R/V Sonne.

The working halves of Cores SO257-18548 and -18571 were initially sampled at 10 cm intervals (1 cm thick half slices of 11 cm core diameter). Additional samples were taken over Termination I (six samples from Core SO257-18548 between 94.5 and 204.5 cm core depth) and Termination II (10 samples from Core SO257-18548 between 456.5 and 576.5 cm core depth) to refine the age model. Four holes were cored at Site U1482 during IODP Expedition 363 (Rosenthal et al., 2018). The working halves from the composite sediment succession (shipboard splice) between 24.76 and 30.22 m composite depth (mcd) were sampled at 20 cm intervals (2 cm thick half slices of ~7 cm core diameter). The sediment succession from Core SO257-18548 and nearby Site U1482 were combined, based on the correlation of the high-resolution X-ray fluorescence (XRF) scanner elemental records. The tie point between these records, corresponding to an age of ~324 ka, is located at 10.84 m in Core SO257-18548 and at 24.97 mcd in Site U1482 (Pei et al., 2021). All samples were oven dried at 40°C and weighed prior to washing over a 63 μm sieve. Residues were oven-dried at 40°C on filter paper, then weighed and sieved into the fractions >315, 315–250, 250–150 and 150–63 μm.

3.3. Chronology

The age models of Cores SO257-18548 and -18571 over the last glacial termination and Holocene are based on 14C accelerator mass spectrometry (AMS) dates obtained from *Globigerinoides ruber* (white) > 250 μm. The age model prior to 21 ka was generated by correlating the benthic foraminiferal $\delta^{18}O$ to the benthic isotope stack LR04 (Lisiecki & Raymo, 2005). Details of the 14C and oxygen isotope stratigraphy of Cores SO257-18548, SO257-18571, and Site U1482 between 24.76 and 30.22 mcd are provided in Pei et al. (2021). We additionally tested the robustness of the age models for the last 25 kyr by correlating our Log(K/Ca) records derived from XRF-scanning to the higher resolution Log(K/Ca) record from Core MD01-2378, which is based on a robust radiometric age model of more than one hundred 14C AMS dates (Kuhnt et al., 2015). This correlation shows that the two approaches provide highly compatible age models for both cores across Termination I (Figure S1 in Supporting Information S1).

3.4. *Globigerinoides Ruber* (White) Stable Isotopes and Mg/Ca

We selected 45–50 well preserved specimens per sample of the planktic foraminifer *Globigerinoides ruber* sensu stricto (white; size fraction 250–315 μm) for paired Mg/Ca and stable isotope analysis. All tests were checked under the microscope for cement encrustations and infillings before being broken into large fragments. Samples were crushed between two glass plates to open all chambers of the tests. Approximately one quarter of the sample material was used for stable isotope analysis. After crushing, samples for isotope analysis were cleaned with ethanol (≥99.7%) for two to three seconds in an ultrasonic bath, decanted and dried at 40°C prior to analysis with a Thermo Finnigan MAT 253 mass spectrometer at the Leibniz Laboratory for Radiometric Dating and Isotope Research, Kiel University, Kiel. The mass spectrometer is coupled to a Kiel-Carbo IV device for automated CO_2 preparation from carbonate samples. Sample reaction was induced by individual acid addition (99% H_3PO_4 at 75°C) under vacuum. The evolved carbon dioxide was analyzed eight times for each individual sample. As documented by the performance of international [NBS19: −2.20‰ VPDB (^{18}O)] and laboratory-internal carbonate standards [Hela1: +2.48‰ VPDB (^{18}O); HB1: −18.10‰ VPDB (^{18}O); SHK: −4.85‰ VPDB (^{18}O)], analytical precision of stable isotope analysis is better than ±0.08‰ for $\delta^{18}O$. Values are calibrated relative to Vienna Pee Dee Belemnite (VPDB) scale.

Mg/Ca was measured on approximately three quarters of the picked *G. ruber* tests. The samples were cleaned of the contaminant phases using the cleaning procedure with a reductive step detailed in Barker et al. (2003) and Martin and Lea (2002). The elemental composition of the foraminiferal calcite was analyzed

with a Spectro Ciros SOP CCD inductively coupled plasma optical emission spectrometer (ICP-OES) at the Institute of Geosciences, Kiel University, Kiel. To control the quality of the measurement and the machine drift over the measuring period, every sixth sample is a calibration standard consisting of the certified reference material ECRM 752-1 with a mean value of 3.821 mmol/mol Mg/Ca (Greaves et al., 2008).

3.5. Mg/Ca Temperature Estimates

Sea surface and mixed-layer temperatures were estimated from *G. ruber* Mg/Ca in down-core and core top samples using the calibration derived from sediment trap samples (Anand et al., 2003):

$$\frac{\mathrm{Mg}}{\mathrm{Ca}} = 0.395 \pm 0.009 \exp\left(0.090 * \mathrm{T}\right)$$

We chose this equation because it has consistently been used for temperature reconstructions in this region (Schröder et al., 2016; Xu et al., 2008, 2006) and yields comparable results to other widely used equations (e.g., Dekens et al., 2002; Figure 4). We compared the results to seasonal and annual mean SST from the World Ocean Atlas (WOA13) and to shipboard thermosalinograph measurements taken during R/V Sonne Cruise SO257 in late May 2017 (Figure 4). Errors in SST reconstructions were calculated by propagating the errors introduced by Mg/Ca measurements and the Mg/Ca temperature calibrations mentioned above, following the approach described in Mohtadi et al. (2014). A comparison of SST based on different calibrations for the two cores and seasonal temperature data is shown in Figure S2a in Supporting Information S1.

3.6. Sea Surface Water $\delta^{18}O$ ($\delta^{18}O_{sw}$) Reconstructions

We calculated $\delta^{18}O_{sw}$ from $\delta^{18}O$ of foraminiferal calcite and Mg/Ca-based temperature estimates of *G. ruber* for near-surface waters in sediment successions from Core SO257-18548, Site U1482 and Core SO257-18571. We applied the equation from Bemis et al. (1998) and added 0.27‰ to convert to Standard Mean Ocean Water (SMOW; Hut, 1987) to calculate $\delta^{18}O_{sw}$ in surface waters:

$$\delta^{18}\mathrm{O_{sw}}\left(\mathrm{SMOW}\right) = 0.27 + \left(\mathrm{T} - 16.5 + 4.8 * \delta^{18}\mathrm{O}_{G.ruber}\left(\mathrm{VPDB}\right)\right)/4.8$$

We applied an ice volume correction of 60% of the original benthic foraminiferal $\delta^{18}O$ variability in Core SO257-18548, Site U1482, and Core SO257-18571 (Pei et al., 2021; Figure S3 in Supporting Information S1). Since the gradient of the original benthic foraminiferal $\delta^{18}O$ between modern and the LGM (1.6‰) exceeds the global mean value of ~1.1‰ (Waelbroeck et al., 2002), we assume that the contribution of deep water temperature accounts for the difference. A comparison of corrected $\delta^{18}O_{sw}$ values for different estimates of the ice volume component in benthic foraminiferal $\delta^{18}O$ is shown in Figure S2b in Supporting Information S1.

4. Results

4.1. Comparison of Temperature Reconstructions and Modern Sea Surface Data

We followed the globally applied calibration equations (Anand et al., 2003; Dekens et al., 2002) to convert *G. ruber* Mg/Ca to SSTs (Figure 4a). We then compared the results to SST reconstructions based on measured $\delta^{18}O_{sw}$ from shipboard CTD of R/V Sonne Cruise SO257 in May 2017 and *G. ruber* $\delta^{18}O$ measurements at the investigated sites (Figure 4d). Additionally, we compared our Mg/Ca-derived SST to seasonal SST from the WOA13 and to SST measured during R/V Sonne Cruise 257 in austral fall (May 2017; Table S1 and Figure S2a in Supporting Information S1). We observe a systematic deviation of the reconstructed temperatures from local annual average temperatures using the global calibration equations. This deviation increases toward the southwestern (south of 23°S latitude) stations, where reconstructed temperatures are in the range of ~25°C, whereas modern local annual average temperatures are substantially cooler (~22°C; Figure 4a). However, temperatures reconstructed with the global calibration equations closely match austral late summer to fall temperatures in this southwestern area (Figure 4b) and SST calculated from *G. ruber* $\delta^{18}O$ and measured $\delta^{18}O_{sw}$ from shipboard CTD water samples. This suggests that the deviation of reconstructed temperatures from annual average SST along the Western Australian Margin is caused by a seasonal bias of *G. ruber* abundances toward the late summer-fall season, when the Leeuwin Current is intensified.

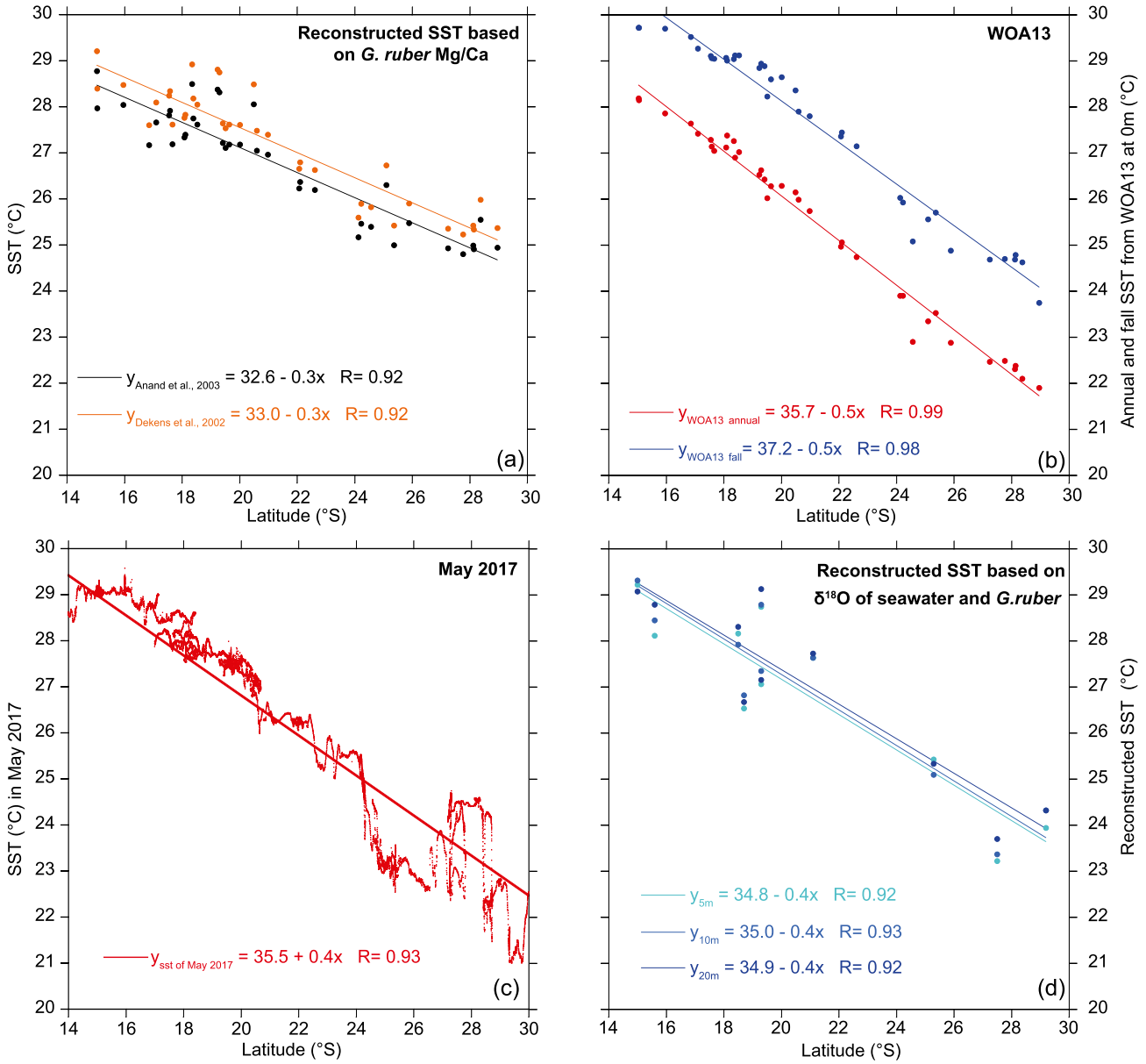

Figure 4. (a) Latitudinal change of *G. ruber* Mg/Ca-derived SST in SO257 core top samples using calibrations of Anand et al. (2003; black dots) and Dekens et al. (2002; orange dots); (b) Latitudinal change of annual average (red dots) and austral late summer/fall (March–May, blue dots) SST at 0 m from WOA13; (c) Latitudinal change of SST from SO257 shipboard thermosalinograph; (d) Latitudinal change of reconstructed SST based on measured $\delta^{18}O_{sw}$ from shipboard CTD of R/V Sonne and *G. ruber* $\delta^{18}O$.

Temperature differences are less pronounced at stations within the IPWP further to the northwest, where the seasonality of SST is reduced and summer SST is close to the annual average. At the northernmost stations SO257-18547 and -18548, modern SST is on average ~29°C during austral summer (January–March) and ~27°C during austral winter (July–September) with an annual average of 28.2°C (Figures 1 and 4; Table S1 in Supporting Information S1). This annual average matches within error the local core-top *G. ruber* Mg/Ca temperatures reconstructed using the global calibration equations (Figure 4a).

4.2. Modern Distribution of *Globigerinoides Ruber* $\delta^{18}O$ Along the Western Australian Margin

Globigerinoides ruber $\delta^{18}O$ measured along the SO257 NE-SW transect increases consistently from a minimum of nearly −3.0‰ at the northeastern end of the transect to values between 1.3‰ and 1.6‰ at the

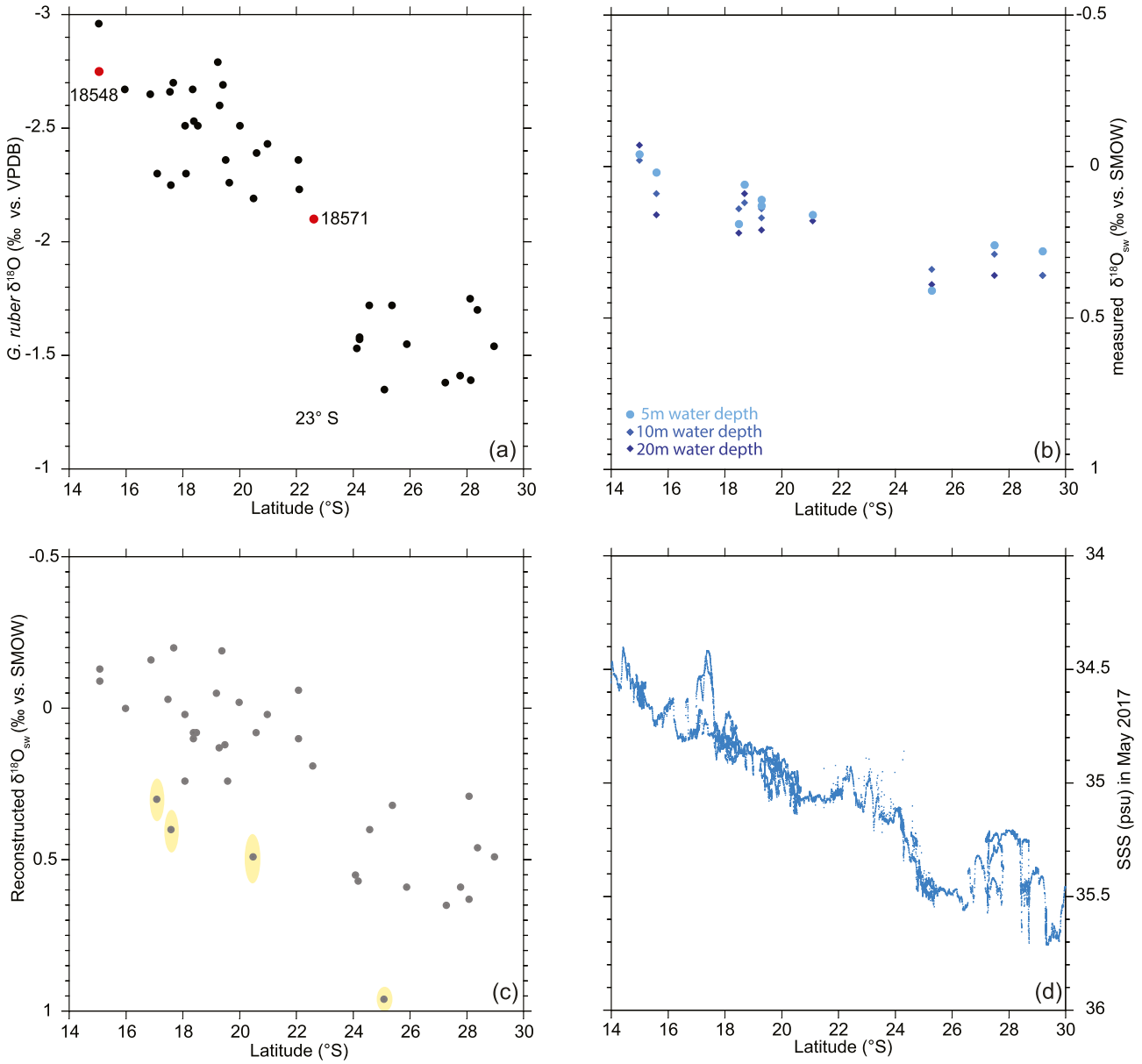

Figure 5. (a) Latitudinal variability in *G. ruber* $\delta^{18}O$ measured in SO257 core top samples; (b) Latitudinal variability in the mixed layer (5, 10, and 20 m water depth) $\delta^{18}O_{sw}$ measured in CTD Niskin bottle water samples in May 2017 during R/V Sonne Cruise SO257; (c) Latitudinal variability in reconstructed $\delta^{18}O_{sw}$ from paired *G. ruber* $\delta^{18}O$ and Mg/Ca-derived SST data; yellow shaded stations probably are influenced by wind-driven and tidal mixing of the upper water column, which commonly occurs in shallow shelf areas; (d) Latitudinal change of SSS from SO257 shipboard thermosalinograph.

southernmost stations (Figure 5). We recognize a distinct break between two clusters of values, a northerly group with $\delta^{18}O$ values of −2.1‰ or lower and a southerly group with values above 1.8‰. The limit between these two groups, which is located offshore the Northwest Cape at 23°S (Figures 3–5), can be defined as the seasonal position of the oceanic front at the southwestern edge of the IPWP.

4.3. Measured and Reconstructed Seasonal and Annual Average Surface $\delta^{18}O_{sw}$: Relation to Seasonal and Annual Average SSS

We reconstructed $\delta^{18}O_{sw}$ from $\delta^{18}O$ and Mg/Ca-based temperature estimates of *G. ruber* in core top samples using the relationship of Bemis et al. (1998). We then compared the results to measured $\delta^{18}O_{sw}$ at 5, 10, and 20 m water depth at 10 stations along the SO257 latitudinal transect (Figures 6a and 6b). Measured $\delta^{18}O_{sw}$

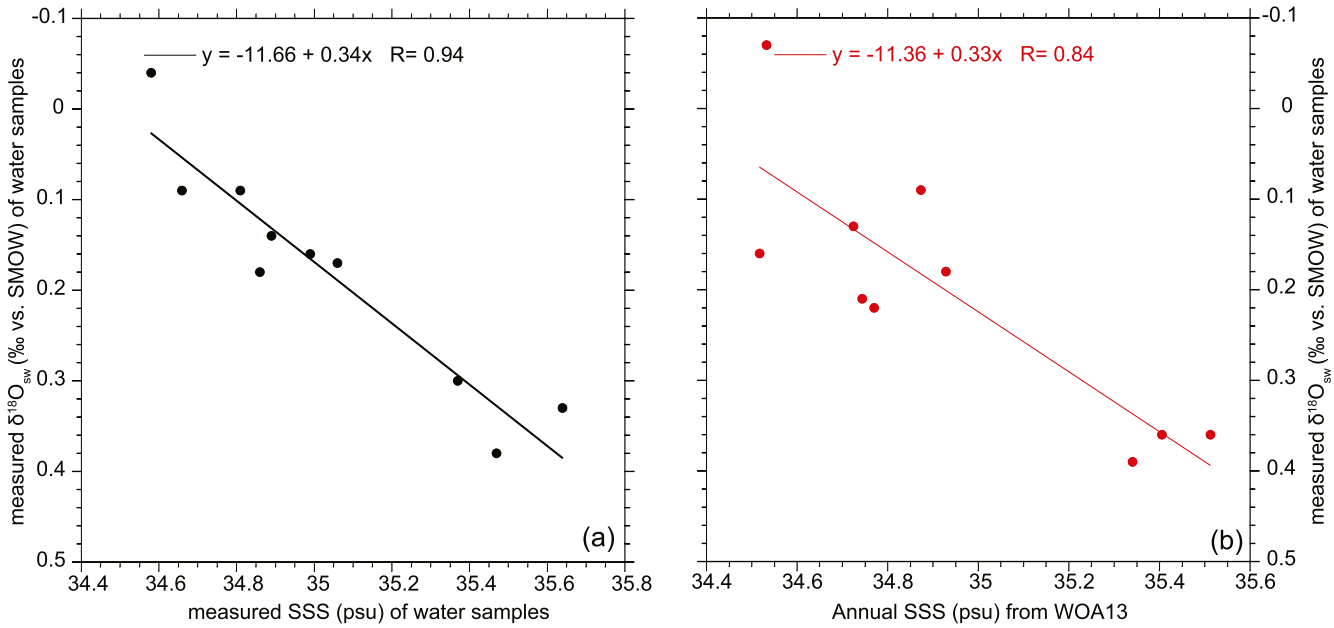

Figure 6. (a) Average SSS versus average $\delta^{18}O_{sw}$ measured in CTD Niskin bottle water samples taken in May 2017 (mean of 5, 10, and 20 m water depth). (b) Annual average SSS (psu) from WOA13 versus average measured $\delta^{18}O_{sw}$ from CTD bottles (mean of 5, 10, and 20 m water depth).

ranges between −0.07‰ at 20 m water depth at the most northeasterly CTD station SO257-18546 (15°S) and 0.36–0.39‰ at 20 m water depth at the three southwestern CTD Station SO257-18577, -18583 and -18590 between 25° and 29°S (Table S2 in Supporting Information S1). Measured $\delta^{18}O_{sw}$ increases steadily southward with a slope of 0.025‰ per degree latitude. By contrast, reconstructed $\delta^{18}O_{sw}$ exhibits a much steeper slope than measured $\delta^{18}O_{sw}$ with an increase of 0.05‰ per degree latitude (Figure 4). The increase with latitude is less uniform and characterized by two distinct clusters with low values north of 23°S and high values south of 23°S. Our data also show a clear $\delta^{18}O_{sw}$-salinity correlation along the Western Australian Margin, indicating that $\delta^{18}O_{sw}$ reconstructions are highly suited to evaluate the amount of monsoonal freshwater flux in this region. The local relationship of measured SSS and $\delta^{18}O_{sw}$ at 5–20 m water depth is:

$$\delta^{18}O_{sw} = -11.66 + 0.34 * SSS$$

which corresponds to a slope of 0.34‰ per psu (Table S2 in Supporting Information S1, Figure 6a). This is in the range of tropical central Pacific mixed layer values and closely matches the relatively steep $\delta^{18}O_{sw}$ per SSS slope in the center of the IPWP near Palau (Conroy et al., 2014, 2017; Morimoto et al., 2002).

4.4. *Globigerinoides Ruber* $\delta^{18}O$ Variability Over the Last 450 kyr

The *G. ruber* $\delta^{18}O$ record displays marked glacial-interglacial variability with values oscillating between −2.75‰ and −0.73‰ in Core SO257-18548 and Site U1482 and between −2.27‰ and −0.47‰ in Core SO257-18571 (Figure 7). In Core SO257-18548 and Site U1482, *G. ruber* $\delta^{18}O$ fluctuates between −1.25‰ and −0.81‰ during MIS 12, then decreases to −2.59‰ during Termination V. Values increase consistently from −2.00‰ to −1.04‰ during MIS 10 and vary between −1.70 and −2.71‰ during MIS 9, increasing to a maximum of −1.06‰ during MIS 8. Values fluctuate between −1.50 and −2.37‰ during MIS 7, reaching a peak of −0.97‰ during MIS 6. After the onset of Termination II, $\delta^{18}O$ decreases sharply to a minimum of −2.75‰ before increasing to reach the highest values (−0.73‰) during the LGM. During Termination I, $\delta^{18}O$ exhibits a decrease from −0.73‰ to −2.61‰. In Core SO257-18571, *G. ruber* $\delta^{18}O$ increases from −2.07‰ to −0.35‰ during mid-MIS 9 and mid-MIS 8, then decreases to −1.91‰ during Termination III. Values oscillate between −0.81‰ and −1.97‰ during MIS 7 and fluctuate between −1.50‰ and −0.60‰ during MIS 6, before decreasing to their lowest value of −2.37‰ during MIS 5e. During the last glacial

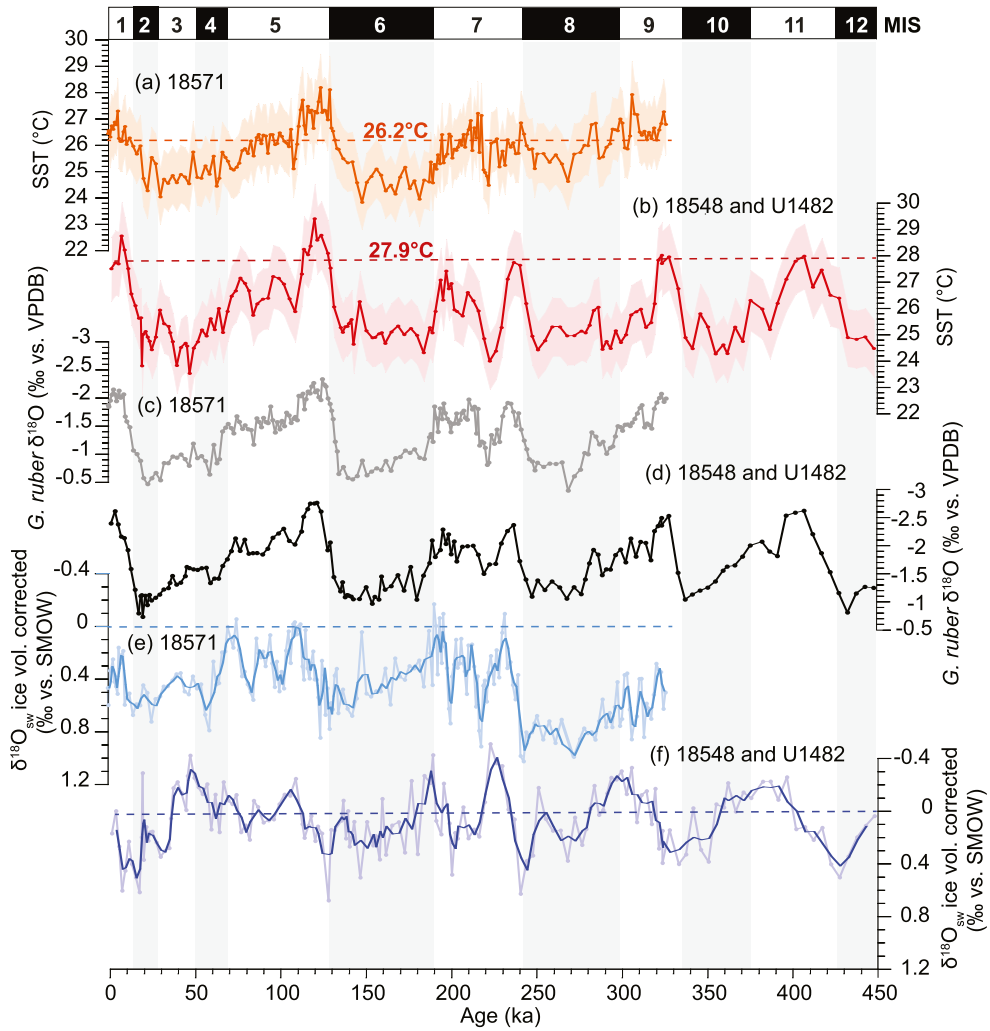

Figure 7. Evolution of sea surface hydrology along the Western Australian Margin over the past 450 kyr. Mg/Ca-derived SST in (a) Core SO257-18571 (orange), (b) Core SO257-18548 and Site U1482 (red), based on calibration from Anand et al. (2003). Envelopes in (a and b) denote uncertainties in SST records estimated by propagating errors, which are ~1°C. Dashed orange and red lines in (a and b) indicate modern reconstructed SST in multicorer core top samples from Sites SO257-18548 and -18571. Planktic $\delta^{18}O$ in (c) Core SO257-18571 (gray), (d) Core SO257-18548 and Site U1482 (black), $\delta^{18}O_{sw}$ in (e) Core SO257-18571 (light blue) with 3 pt running average (blue), (f) Core SO257-18548 and Site U1482 (light blue) with 3 pt running average (dark blue). Blue dashed lines in (e and f) mark 0. SMOW: standard mean ocean water; MIS Marine Isotope Stage. Light gray shading indicates glacial MIS following Lisiecki and Raymo (2005).

cycle, values increase once more to reach a maximum of −0.47‰ during the LGM. Holocene values exhibit a minimum of −2.15‰.

4.5. SST Variability Over the Last 450 kyr

Globigerinoides ruber Mg/Ca varies between 3.29 and 5.57 mmol/mol over the past 450 kyr in Core SO257-18548 and Site U1482, corresponding to SSTs between 23.5°C and 29.4°C (Figure 7), in comparison to the modern annual SST average of 28.2°C at this location (WOA13; Table S1 in Supporting Information S1). During MIS 6 to 12, SSTs show marked glacial-interglacial variability, fluctuating between ~24°C and 28°C. Peak temperatures of 29.4°C and 28.8°C were reached during MIS 5e and the early Holocene, respectively. The glacial-interglacial SST difference is ~4°C for Terminations I and II. During Termination II, SSTs exhibit a sharp increase, rising from 25.3°C to a maximum of 29.4°C during MIS 5e. SSTs decreased to their

lowest values (~23°C) during MIS3 and the LGM, then rose to the second maximum of 28.8°C during the early Holocene (Figure 7).

In Core SO257-18571, the glacial-interglacial temperature contrast is lower, which is mainly due to lower interglacial SSTs (Figure 7a). Mg/Ca fluctuates between 3.38 and 4.99 mmol/mol and SSTs range from 23.8°C to 28.2°C, in comparison to the modern annual SST average of 25.0°C at this location (WOA13; Table S1 in Supporting Information S1). During MIS 6 to 9, SSTs show glacial-interglacial variability between 23.8°C and 27.9°C, which is less pronounced than in Core SO257-18548 and Site U1482. During MIS 5e, SSTs were ~2°C higher than today, fluctuating between ~27°C and 28°C. An abrupt cooling by ~2°C occurred at the end of MIS 5e followed by an overall cooling trend from ~26°C to ~24°C during MIS 5d to MIS 2. During Termination I, SSTs display a steady rise, reaching 27.3°C in the Holocene, which is ~1°C lower than during MIS 5e (Figure 7).

4.6. Seawater Oxygen Isotope Composition and Salinity Variability Over the Last 450 kyr

Today, the northeasterly Core SO257-18548 and Site U1482, which are more directly influenced by river discharge from the Australian monsoon region and advection of freshwater from the Indonesian archipelago, exhibit annual average core top $\delta^{18}O_{sw}$ of 0.17‰ (reconstructed from core top *G. ruber* Mg/Ca-derived temperatures and *G. ruber* $\delta^{18}O$) and seasonally lighter seawater $\delta^{18}O_{sw}$ of −0.04‰ in May 2017 (direct measurement of seawater sampled with the CTD Niskin bottle at 5 m water depth). The southwesterly Core SO257-18571 displays an annual average $\delta^{18}O_{sw}$ of 0.47‰ and a seasonal value of 0.17‰ in May 2017, resulting in seasonal offsets between ~0.2‰ and 0.3‰ and regional offsets in the same order of magnitude for annual average and the post-monsoonal season. Mean $\delta^{18}O_{sw}$ in Core SO257-18571 (0.43‰) is ~0.3‰ higher than in Core SO257-18548 and Site U1482 (0.07‰) over the last four glacial cycles, corresponding to a salinity, which is higher by as much as ~1 psu (Figure 7). Today, the annual average salinity difference at these stations is 0.5‰ and the salinity difference in austral fall 2017 was in the same order of magnitude (Table S2 in Supporting Information S1). The highest $\delta^{18}O_{sw}$ and salinities occurred during glacials and in the early phase of glacial terminations. Lowest salinity is synchronous in the early part of interglacials at both sites with the exceptions of MIS 3, which is characterized by low "interglacial" values ($\delta^{18}O_{sw}$ between −0.2‰ and −0.4‰) in Core SO257-18548 and Site U1482. In contrast, Core SO257-18571 exhibits a high "glacial" salinity (ice volume corrected $\delta^{18}O_{sw}$ between 0.4‰ and 0.8‰).

5. Discussion

5.1. Factors Influencing Seasonal and Annual SST and SSS Reconstructions Along the Western Australian Margin

5.1.1. Seasonality in *G. Ruber* Distribution

Reconstruction of $\delta^{18}O_{sw}$/salinity is usually based on temperature correction of *G. ruber* $\delta^{18}O$ with Mg/Ca-derived SST reconstructed with globally applicable calibrations such as Anand et al. (2003) and Dekens et al. (2002). However, we recognized that reconstructed temperatures in our core top data set overestimate annual average temperatures at the southwestern (cooler) stations by ~2°C–3°C (Figure 4). Warm temperatures that match Mg/Ca-derived estimates at these southwestern locations are only reached during austral fall (March–May), when the warm Leeuwin Current is active (Fieux et al., 2005). A bias by dissolution or carbonate ion effects can be excluded, since warm temperatures at the most northeastern stations are accurately reconstructed and deviations toward higher Mg/Ca and warmer temperatures only occur at the southwestern stations. A potential cause for this discrepancy is a seasonal bias of the *G. ruber* population density toward the warm season at the cooler southwestern stations (Figure S2c in Supporting Information S1). This bias may be accentuated by the fact that *G. ruber* tests are carried southward from the warm area east of the Northwest Cape to the cooler waters along the Western Australian Margin with the strengthening Leeuwin Current, as is the case for clay minerals (Gingele et al., 2001).

To evaluate the impact of this seasonal bias on our SST reconstructions, we compared the results of global Mg/Ca calibrations to measured annual average and seasonal SST from WOA13 and shipboard CTD and thermosalinograph measurements in May 2017 at 40 stations sampled during R/V Sonne Cruise SO257

along the Western Australian Margin (Figure S2a in Supporting Information S1). This comparison shows that global Mg/Ca calibrations closely match the SSTs of the post-monsoonal WOA13 fall data set and temperatures measured in the near-surface CTD and thermosalinograph measurements in May 2017 (Figure 4, Figure S2a in Supporting Information S1). Using the local annual average temperatures as a base for regional calibrations results in temperature estimates that are ~2°C cooler and exhibit slightly higher glacial-interglacial temperature gradients (Figure S2b in Supporting Information S1). Thus, we use the calibration of Anand et al. (2003) to estimate downcore SST, since seasonal population dynamics of *G. ruber* along the Western Australian Margin are not known over the last four glacial cycles. However, this approach may lead to slightly amplified glacial-interglacial gradients in reconstructed SST and SSS, since the seasonality of *G. ruber* populations may have been enhanced during glacials.

5.1.2. Temporal and Spatial Variability of the Oceanic Front at the Southeastern Margin of the IPWP

The most significant feature in the mixed layer temperature record along the SO257 latitudinal transect is the rapid southward decrease in Mg/Ca-derived SST, associated with a salinity ($\delta^{18}O_{sw}$) increase at the southeastern margin of the IPWP (Figures 4 and 5). This steep gradient, which represents the seasonal position of the oceanic front at the southeastern margin of the IPWP, was identified between 23° and 24°S toward the end of May to early June during previous cruises (e.g., Weller et al., 2011). This temperature gradient is associated with southward shallowing of the thermocline and intensified current activity, formation of eddies, enhanced upper ocean mixing and increased nutrient levels in surface water masses (Thompson & Richards, 2011; Weller et al., 2011). Although this boundary was situated ~1° south of Station SO257-18571 at the end of May 2017 during R/V Sonne Cruise SO257, the site would have been bathed by cooler, nutrient rich surface water masses of southern origin during austral winter. Temperature and salinity reconstructions at this site are, thus, well suited to monitor the spatial expansion and contraction of the IPWP and changes in the related intensity of the warm Leeuwin Current over the last glacial cycles.

5.2. Phasing of Deglacial Warming to Atmospheric Carbon Dioxide Increase and Southern Hemisphere Insolation Forcing

Centennial-scale SST records in combination with AMS 14C dates tuned to independently dated deglacial 14C plateaus previously suggested that deglacial tropical warming in the Indonesian seas and off northwestern Australia led atmospheric CO_2 measured in Antarctic ice cores by ~500 yr during Termination I (Sarnthein et al., 2011; Schröder et al., 2018). This relatively short lead is not resolved in our millennial-scale SST records, and the onset of deglacial warming and atmospheric pCO_2 rise at the beginning of Terminations I, II, III, and IV appears coeval in Cores SO257-18571 and SO257-18548 and Site U1482 (Figure 8). However, the distinct temperature maxima at the end of terminations and early part of interglacials generally lag behind atmospheric pCO_2 maxima (Table S3 in Supporting Information S1). In both cores, cross-spectral analyses between pCO_2 and SST reveal high coherence and a consistent lag of SST by 0.6–0.7 kyr (Figure S4 in Supporting Information S1). Possible explanations for this phase lag are: (a) the time-lag could be a result of a change in the seasonality of *G. ruber* as an adaption to warming and/or monsoon intensification. (b) The ice core pCO_2 and SST records are based on different time scales. Our SST times series are derived from tuning of the benthic foraminiferal isotope records to the LR04 stack, which may induce a time lag to the atmospheric pCO_2 record due to the travel time of the $\delta^{18}O$ signal to the site location, estimated to be in the order of 0.5–1 kyr (Matsumoto, 2007; Stott et al., 2007). The high covariance and, within the limitation of our age models, consistent phase relationship between our SST records, atmospheric pCO_2 in Antarctic ice core records and maxima in monsoonal terrigenous discharge from the Australian continent (Figure 8; Figure S5 and Table S3 in Supporting Information S1) support a direct connection between these three variables during glacial terminations.

The atmospheric pCO_2, SST, and monsoonal runoff maxima at the end of glacial terminations also coincide with precession minima at obliquity maxima. This orbital configuration results in a combination of maximum Northern Hemisphere summer insolation with maximum cross-equatorial heat transfer, due to obliquity induced steepening of summer inter-tropical latitudinal insolation gradients (Bosmans et al., 2014; Davis & Brewer, 2009; Rossignol-Strick, 1983). In addition to Northern Hemisphere summer insolation, Southern Hemisphere insolation may have contributed to warming in the southeastern Indian Ocean.

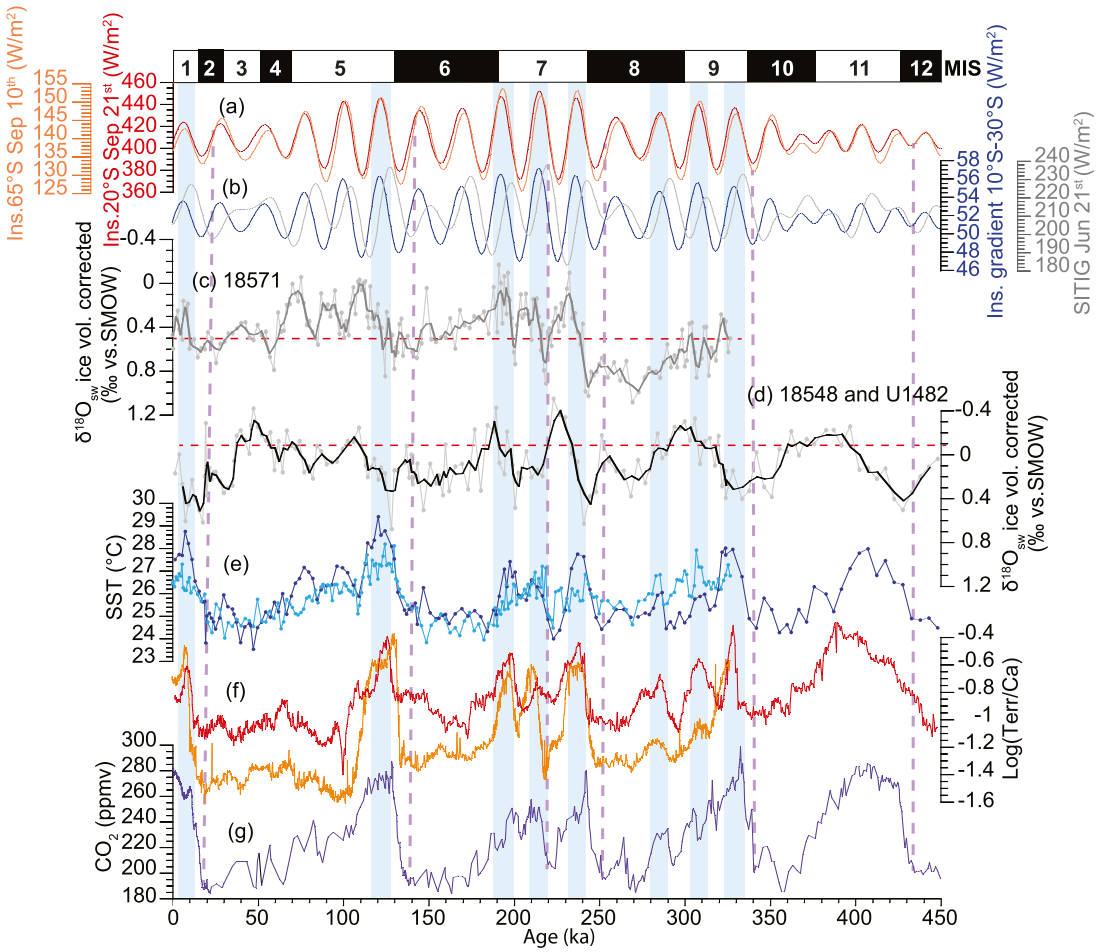

Figure 8. Comparison of temperature and terrigenous discharge in Core SO257-18571, Core SO257-18548 and Site U1482 with insolation and greenhouse gas forcing. Reconstructed SST is based on the calibration of Anand et al. (2003). (a) September 21, insolation at 20°S and September 10 insolation at 65°S. (b) Insolation gradient between 10° and 30°S; SITIG: boreal summer inter-tropical insolation gradient. (c) Ice volume corrected $\delta^{18}O_{sw}$ in Core SO257-18571 (light gray) with 3 pt running average (dark gray). (d) Ice volume corrected $\delta^{18}O_{sw}$ in Core SO257-18548 and Site U1482 (light gray) with 3pt running average (black). (e) SST from Core SO257-18571 (light blue), Core SO257-18548 and Site U1482 (blue), (f) XRF-scanner derived Log(Terr/Ca) from Core SO257-18571 (orange), Core SO257-18548 and Site U1482 (red) from Pei et al. (2021). (g) EPICA Dome C (EDC) ice core CO_2 record (Lüthi et al., 2008). Blue shading indicates precessional insolation maxima that coincide with elevated SST, increased monsoonal discharge and high atmospheric pCO_2. Horizontal dashed red lines indicate average ice volume corrected $\delta^{18}O_{sw}$ from Core SO257-18571 and from Core SO257-18548 and Site U1482. Vertical purple dashed lines indicate onset of deglacial atmospheric pCO_2 and tropical SST rise, which are in phase on millennial-scale time resolution.

Austral spring insolation (daily insolation on September 10 at 65°S) in combination with the duration of austral summer (days on which diurnal average insolation exceeds 250 W/m² at 77°S) may have triggered Southern Hemisphere warming (as recorded in Antarctic ice cores) in phase with Northern Hemisphere warming (Huybers, 2009). The variability of austral spring insolation and the duration of austral summer over the last 450 kyr exhibit close similarities to Northern Hemisphere precessional summer insolation (daily insolation on June 21 at 65°N; Huybers, 2009). A possible underlying mechanism is that enhanced austral spring insolation promoted decreases in the sea ice cover around Antarctica and increases in the heat transport into the interior of Antarctica with repercussions for the entire Southern Hemisphere climate (Timmermann et al., 2009). The relative importance of these mechanisms to explain Southern Hemisphere warming during summer insolation minima is still an issue of intense debate. Atmospheric carbon dioxide, which is rapidly mixed in the atmosphere, appears to play a major role in triggering coeval temperature changes in both hemispheres, although the forcing mechanisms that drive atmospheric pCO_2 variability on orbital time scales are still unclear. Overall, our records suggest that the steep rise in atmospheric pCO_2 and Southern Hemisphere SST in the late phase of glacial terminations in combination with high Southern

Hemisphere spring insolation and extended duration of Southern Hemisphere summers contributed to the intensification of the Australian monsoon.

5.3. Hydrological Variability During the Last Four Glacial Cycles

Today, the seasonality of SSS along the Western Australian Margin is mainly driven by the advection of low salinity waters originating from the Indonesian archipelago via the ITF and by local precipitation and eddy fluxes along the pathway of the Leeuwin Current that freshen the mixed layer (Pattiaratchi, 2006; Thompson & Richards, 2011; N. Zhang et al., 2016). Salinity fronts migrate seasonally and interannually with the movement of the ITCZ and the El Niño-Southern Oscillation-modulated surface component of the ITF (Hu et al., 2019; N. Zhang et al., 2016). The strength of the advected freshwater flux is largely dependent on the intensity of the tropical convective rainfall over the Indonesian Maritime Continent, but is also affected by intense vertical mixing in the Banda Sea before reaching the Timor Sea. Differences in the amount and seasonality of precipitation and riverine discharge as well as in the transport and mixing along the ITF pathway, thus, contribute to a complex salinity signal in the eastern Indian Ocean. These intricate interactions ultimately drive variability of $\delta^{18}O_{sw}$ and salinity along the Western Australian Margin on seasonal (Condie & Dunn, 2006), interannual (Cahyarini et al., 2014; Hu et al., 2019) and orbital timescales (Spooner et al., 2011).

The ice volume corrected $\delta^{18}O_{sw}$ record in the southwestern Core SO257-18571 exhibits clear glacial-interglacial variability with glacial values between 0.4‰ and 0.8‰ during MIS 2–4 and MIS 6 (Figure 8). This marked glacial-interglacial contrast suggests that the southwestern Core SO257-18571 was situated in cooler and more saline water masses, remaining south of the IPWP southwestern front during glacials. Glacial values during MIS 8 were even higher (between 0.8‰ and 1.2‰), indicating a less expanded IPWP and weaker Leeuwin Current. By contrast, the $\delta^{18}O_{sw}$ record in the northeastern location (Core SO257-18548 and Site U1482) exhibits subdued glacial-interglacial variability and is characterized by higher frequency and lower amplitude fluctuations between maxima of ∼0.6‰ and minima of ∼–0.4‰. During the last glacial cycle, for instance, $\delta^{18}O_{sw}$ displayed comparable values during the early part of MIS 3 and the Holocene. These low glacial-interglacial differences in temperature and salinity suggest that the northeastern part of the Western Australian Margin remained under the influence of IPWP water masses, even during glacials, throughout the past 450 kyr. At both coring sites, however, the glacial-interglacial contrast in ice volume corrected $\delta^{18}O_{sw}$ corresponding to salinity decreases whereas the temperature contrast increases during the last two glacial cycles (Figure 8). This may be due to changes in the geometry of the Leeuwin Current system and its interaction with the South Indian Countercurrent and the Western Australian Current.

The overall higher SSS during glacials at Site SO257-18571 suggests drier conditions over the entire Maritime Continent and along the pathway of the ITF. Low salinities and unusually warm temperatures in the early phase of interglacials at this location bear similarities to modern conditions during "Ningaloo Niño" events (Feng et al., 2013). During these events, low-salinity anomalies in the Indonesian seas and along the Western Australian Margin, caused by anomalous precipitation in the region and ITF freshwater advection, are carried southward by the Leeuwin Current. These warming and freshening anomalies that are associated with prolonged La Niña periods in the tropical Pacific have been more commonly observed in the ITF and the Leeuwin Current over the past few decades (Feng et al., 2015). Ningaloo-Niño type warming and freshening events seem to become more frequent and intense at elevated pCO_2 levels and may have also contributed to the unusually warm and wet conditions off Australia during intervals of peak pCO_2 levels following glacial terminations.

5.4. Relative Influence of ITF and Indonesian-Australian Monsoon on Regional Hydrology

The contrasting positions of the two sediment successions in relation to the IPWP are reflected by different responses of SST to precessional insolation and atmospheric pCO_2 forcing (Figures S4 and S5 in Supporting Information S1). Within the IPWP (Core SO257-18548 and Site U1482), SST is highly coherent with both precession (coherence: 0.92) and pCO_2 (coherence: 0.94) and exhibits a phase lag of 5.1 kyr to precession and a smaller phase lag of 0.6 kyr to pCO_2 (Figure S5a in Supporting Information S1) which suggests a more direct response of SST to atmospheric greenhouse gas forcing (Lea et al., 2006; Medina-Elizalde &

Lea, 2005). By contrast, SST south of the IPWP (Site SO257-18571) exhibits low coherence (0.45) with precession (Figure S4d in Supporting Information S1), whereas ice-volume corrected $\delta^{18}O_{sw}$, a direct proxy for salinity variability, is highly coherent (0.83 in Core SO257-18548 and Site U1482 and 0.72 in Core SO257-18571) and in phase with precession at both sites. This similarity in ice-volume corrected $\delta^{18}O_{sw}$ suggests that the transfer of the salinity signal from the Indonesian seas to the eastern Indian Ocean via the ITF and Leeuwin Current remained consistent over orbital timescales.

However, this temporal variability in circulation-driven salinity is remarkably different from the imprint of local monsoonal precipitation and discharge on the sedimentation along the Western Australian Margin (Figure 8). Monsoonal sediment discharge from the Australian continent, expressed as Log(Terr/Ca), in Core SO257-18548 and Site U1482, which are directly exposed to monsoonal discharge from the Fitzroy River (Figure S4c in Supporting Information S1) is highly coherent (coherence: 0.77) to precession with a consistent phase lag of 5.1 kyr. Whereas SSS variability at this site represents an integrated signal of monsoonal precipitation and runoff as well as intense advective mixing along the ITF pathway, the terrigenous sediment flux more directly captures the local monsoonal precipitation and runoff signal from the Australian continent (e.g., Milliman & Farnsworth, 2011).

6. Conclusions

Temperature, salinity, and oxygen isotope analyses of seawater in combination with stable isotope and Mg/Ca analysis of near-surface dwelling planktic foraminifers in sediment core tops from a transect along the Western Australian Margin between 15° and 27°S allow monitoring of spatial variations of the southwestern edge of the IPWP. Today, the southwestern edge of the IPWP is characterized by a sharp decrease in SST and concurrent increases in salinity and planktic $\delta^{18}O$ between 23° and 24°S off Northwest Cape during the post-monsoonal austral fall (May). Reconstructed mixed layer temperatures and salinities over the last 450 kyr in two sediment successions at the southwestern edge of the IPWP (Site SO257-18548/U1482 at 15°S) and southwest of the IPWP (Site SO257-18571 at 22°S) suggest that even during glacials the northeastern region remained influenced by IPWP water masses. By contrast, the southwestern Site SO257-18571 was located in colder, more saline and nutrient-rich mixed layer water masses, south of the IPWP front during glacials. Coherence and phase relationship between insolation forcing, atmospheric pCO_2, SST, and monsoonal intensity (terrigenous discharge) suggest that global greenhouse gas concentrations and Southern Hemisphere spring insolation strongly influenced the spatial extent of the IPWP in the Southern Hemisphere and Australian monsoonal climate. However, our results additionally indicate that sea surface hydrology (salinity) along the Western Australian represents an integrated signal of regional monsoonal precipitation and intense advective mixing along the ITF pathway.

Data Availability Statement

Data presented in this study are available from the Data Publisher for Earth & Environmental Science at https://doi.pangaea.de/10.1594/PANGAEA.931770.

Acknowledgments
This research used data and samples provided by the IODP. The authors are grateful to the captain, crew, and shipboard scientific parties of R/V Sonne 257 and IODP Expedition 363 for all their efforts. This study was funded by the German Federal Ministry of Education and Research (Grant SO-257, WACHEIO, 03G0257A). Renjie Pei gratefully acknowledges the funding from the China Scholarship Council towards her PhD at Kiel University. The authors thank Dieter Garbe-Schönberg and Karen Bremer for ICP-OES Mg/Ca analyses assistance. The authors thank to anonymous reviewers for constructive, critical comments that helped us to improve the manuscript.
Open access funding enabled and organized by Projekt DEAL.

References

Anand, P., Elderfield, H., & Conte, M. H. (2003). Calibration of Mg/Ca thermometry in planktonic foraminifera from a sediment trap time series. *Paleoceanography*, *18*(2). https://doi.org/10.1029/2002pa000846

Ayliffe, L. K., Gagan, M. K., Zhao, J. X., Drysdale, R. N., Hellstrom, J. C., Hantoro, W. S., et al. (2013). Rapid interhemispheric climate links via the Australasian monsoon during the last deglaciation. *Nature Communications*, *4*(2908), 1–6. https://doi.org/10.1038/ncomms3908

Barker, S., Greaves, M., & Elderfield, H. (2003). A study of cleaning procedures used for foraminiferal Mg/Ca paleothermometry. *Geochemistry, Geophysics, Geosystems*, *4*(9), 1–20. https://doi.org/10.1029/2003GC000559

Bemis, B. E., Spero, H. J., Bijma, J., & Lea, D. W. (1998). Reevaluation of the oxygen isotopic composition of planktonic foraminifera: Experimental results and revised paleotemperature equations. *Paleoceanography*, *13*(2), 150–160. https://doi.org/10.1029/98PA00070

Bosmans, J. H. C., Drijfhout, S. S., Tuenter, E., Hilgen, F. J., & Lourens, L. J. (2014). Response of the North African summer monsoon to precession and obliquity forcings in the EC-Earth GCM. *Climate Dynamics*, *44*(1–2), 279–297. https://doi.org/10.1007/s00382-014-2260-z

Bosmans, J. H. C., Erb, M. P., Dolan, A. M., Drijfhout, S. S., Tuenter, E., Hilgen, F. J., et al. (2018). Response of the Asian summer monsoons to idealized precession and obliquity forcing in a set of GCMs. *Quaternary Science Reviews*, *188*, 121–135. https://doi.org/10.1016/j.quascirev.2018.03.025

Broccoli, A. J., Dahl, K. A., & Stouffer, R. J. (2006). Response of the ITCZ to Northern Hemisphere cooling. *Geophysical Research Letters*, *33*(1), 1–4. https://doi.org/10.1029/2005GL024546

Cahyarini, S. Y., Pfeiffer, M., Nurhati, I. S., Aldrian, E., Dullo, W. C., & Hetzinger, S. (2014). Twentieth-century sea surface temperature and salinity variations at Timor inferred from paired coral $\delta^{18}O$ and Sr/Ca measurements. *Journal of Geophysical Research: Oceans*, *119*(7), 4593–4604. https://doi.org/10.1002/2013JC009594

Chiang, J. C. H., Biasutti, M., & Battisti, D. S. (2003). Sensitivity of the Atlantic Intertropical Convergence Zone to last glacial maximum boundary conditions. *Paleoceanography*, *18*(4), 1–18. https://doi.org/10.1029/2003PA000916

Chiang, J. C. H., & Bitz, C. M. (2005). Influence of high-latitude ice cover on the marine Intertropical Convergence Zone. *Climate Dynamics*, *25*(5), 477–496. https://doi.org/10.1007/s00382-005-0040-5

Chiang, J. C. H., Fang, Y., & Chang, P. (2008). Interhemispheric thermal gradient and tropical Pacific climate. *Geophysical Research Letters*, *35*(14), 2–6. https://doi.org/10.1029/2008GL034166

Chiang, J. C. H., & Friedman, A. R. (2012). Extratropical cooling, interhemispheric thermal gradients, and tropical climate change. *Annual Review of Earth and Planetary Sciences*, *40*, 383–412. https://doi.org/10.1146/annurev-earth-042711-105545

Church, J. A., Cresswell, G. R., & Godfrey, J. S. (1989). The Leeuwin Current. In S. J. Neshyba, C. N. K. Mooers, R. L. Smith, & R. T. Barber (Eds.), *Poleward flows along Eastern Ocean boundaries* (pp. 230–254). Springer-Verlag. https://doi.org/10.1007/978-1-4613-8963-7_16

Claussen, M., Ganopolski, A., Brovkin, V., Gerstengarbe, F. W., & Werner, P. (2003). Simulated global-scale response of the climate system to Dansgaard/Oeschger and Heinrich events. *Climate Dynamics*, *21*(5–6), 361–370. https://doi.org/10.1007/s00382-003-0336-2

Condie, S. A., & Dunn, J. R. (2006). Seasonal characteristics of the surface mixed layer in the Australasian region: Implications for primary production regimes and biogeography. *Marine and Freshwater Research*, *57*(6), 569–590. https://doi.org/10.1071/MF06009

Conroy, J. L., Cobb, K. M., Lynch-Stieglitz, J., & Polissar, P. J. (2014). Constraints on the salinity-oxygen isotope relationship in the central tropical Pacific Ocean. *Marine Chemistry*, *161*, 26–33. https://doi.org/10.1016/j.marchem.2014.02.001

Conroy, J. L., Thompson, D. M., Cobb, K. M., Noone, D., Rea, S., & Legrande, A. N. (2017). Spatiotemporal variability in the $\delta^{18}O$-salinity relationship of seawater across the tropical Pacific Ocean. *Paleoceanography*, *32*, 484–497. https://doi.org/10.1002/2016PA003073

Cresswell, G. R., & Peterson, J. L. (1993). The Leeuwin Current south of Western Australia. *Marine and Freshwater Research*, *44*(2), 285–303. https://doi.org/10.1071/MF9930285

Davis, B. A. S., & Brewer, S. (2009). Orbital forcing and role of the latitudinal insolation/temperature gradient. *Climate Dynamics*, *32*(2–3), 143–165. https://doi.org/10.1007/s00382-008-0480-9

De Deckker, P., Barrows, T. T., & Rogers, J. (2014). Land-sea correlations in the Australian region: Post-glacial onset of the monsoon in northwestern Western Australia. *Quaternary Science Reviews*, *105*, 181–194. https://doi.org/10.1016/j.quascirev.2014.09.030

Deininger, M., McDermott, F., Cruz, F. W., Bernal, J. P., Mudelsee, M., Vonhof, H., et al. (2020). Inter-hemispheric synchroneity of Holocene precipitation anomalies controlled by Earth's latitudinal insolation gradients. *Nature Communications*, *11*(1), 1–9. https://doi.org/10.1038/s41467-020-19021-3

Dekens, P. S., Lea, D. W., Pak, D. K., & Spero, H. J. (2002). Core top calibration of Mg/Ca in tropical foraminifera: Refining paleotemperature estimation. *Geochemistry, Geophysics, Geosystems*, *3*(4), 1–29. https://doi.org/10.1029/2001gc000200

Denniston, R. F., Wyrwoll, K. H., Asmerom, Y., Polyak, V. J., Humphreys, W. F., Cugley, J., et al. (2013). North Atlantic forcing of millennial-scale Indo-Australian monsoon dynamics during the last glacial period. *Quaternary Science Reviews*, *72*, 159–168. https://doi.org/10.1016/j.quascirev.2013.04.012

Eroglu, D., McRobie, F. H., Ozken, I., Stemler, T., Wyrwoll, K. H., Breitenbach, S. F. M., et al. (2016). See-saw relationship of the Holocene East Asian-Australian summer monsoon. *Nature Communications*, *7*, 1–7. https://doi.org/10.1038/ncomms12929

Feng, M., Benthuysen, J., Zhang, N., & Slawinski, D. (2015). Freshening anomalies in the Indonesian Throughflow and impacts on the Leeuwin Current during 2010–2011. *Geophysical Research Letters*, *42*(20), 8555–8562. https://doi.org/10.1002/2015GL065848

Feng, M., McPhaden, M. J., Xie, S. P., & Hafner, J. (2013). La Niña forces unprecedented Leeuwin Current warming in 2011. *Scientific Reports*, *3*(1), 1–9. https://doi.org/10.1038/srep01277

Feng, M., Waite, A. M., & Thompson, P. A. (2009). Climate variability and ocean production in the Leeuwin Current system off the west coast of Western Australia. *Journal of the Royal Society of Western Australia*, *92*(2), 67–81.

Field, E., McGowan, H. A., Moss, P. T., & Marx, S. K. (2017). A late Quaternary record of monsoon variability in the northwest Kimberley, Australia. *Quaternary International*, *449*, 119–135. https://doi.org/10.1016/j.quaint.2017.02.019

Fieux, M., Molcard, R., & Morrow, R. (2005). Water properties and transport of the Leeuwin Current and Eddies off Western Australia. *Deep-Sea Research Part I Oceanographic Research Papers*, *52*(9), 1617–1635. https://doi.org/10.1016/j.dsr.2005.03.013

Gallagher, S. J., Wallace, M. W., Li, C. L., Kinna, B., Bye, J. T., Akimoto, K., & Torii, M. (2009). Neogene history of the West Pacific Warm Pool, Kuroshio, and Leeuwin currents. *Paleoceanography*, *24*(1). https://doi.org/10.1029/2008PA001660

Gingele, F. X., De Deckker, P., & Hillenbrand, C. D. (2001). Late Quaternary fluctuations of the Leeuwin Current and palaeoclimates on the adjacent land masses: Clay mineral evidence. *Australian Journal of Earth Sciences*, *48*(6), 867–874. https://doi.org/10.1046/j.1440-0952.2001.00905.x

Gordon, A. L., Huber, B. A., Metzger, E. J., Susanto, R. D., Hurlburt, H. E., & Adi, T. R. (2012). South China Sea Throughflow impact on the Indonesian Throughflow. *Geophysical Research Letters*, *39*(11), 1–7. https://doi.org/10.1029/2012GL052021

Greaves, M., Caillon, N., Rebaubier, H., Bartoli, G., Bohaty, S., Cacho, I., et al. (2008). Interlaboratory comparison study of calibration standards for foraminiferal Mg/Ca thermometry. *Geochemistry, Geophysics, Geosystems*, *9*(8), 1–27. https://doi.org/10.1029/2008GC001974

Holbourn, A., Kuhnt, W., Kawamura, H., Jian, Z., Grootes, P., Erlenkeuser, H., & Xu, J. (2005). Orbitally paced paleoproductivity variations in the Timor Sea and Indonesian Throughflow variability during the last 460 kyr. *Paleoceanography*, *20*(3), 1–18. https://doi.org/10.1029/2004PA001094

Holbourn, A., Kuhnt, W., & Xu, J. (2011). *Indonesian Throughflow variability during the last 140 ka: The Timor Sea outflow* (Vol. *355*, pp. 283–303). Geological Society Special Publication. https://doi.org/10.1144/SP355.14

Hu, S., Zhang, Y., Feng, M., Du, Y., Sprintall, J., Wang, F., et al. (2019). Interannual to decadal variability of upper-ocean salinity in the southern Indian Ocean and the role of the Indonesian Throughflow. *Journal of Climate*, *32*(19), 6403–6421. https://doi.org/10.1175/JCLI-D-19-0056.1

Hut, G. (1987). *Consultants' group meeting on stable isotope reference samples for geochemical and hydrological investigations*. International Atomic Energy Agency (IAEA).

Huybers, P. (2009). Antarctica's Orbital Beat. *Science*, *325*(5944), 1085–1086. https://doi.org/10.1126/science.1176186

Huybers, P., & Denton, G. (2008). Antarctic temperature at orbital timescales controlled by local summer duration. *Nature Geoscience*, *1*(11), 787–792. https://doi.org/10.1038/ngeo311

Ishiwa, T., Yokoyama, Y., Reuning, L., McHugh, C. M., De Vleeschouwer, D., & Gallagher, S. J. (2019). Australian summer monsoon variability in the past 14,000 yr revealed by IODP Expedition 356 sediments. *Progress in Earth and Planetary Science*, *6*(1). https://doi.org/10.1186/s40645-019-0262-5

Kida, S., Richards, K. J., & Sasaki, H. (2019). The fate of surface freshwater entering the Indonesian Seas. *Journal of Geophysical Research: Oceans*, *124*, 3228–3245. https://doi.org/10.1029/2018JC014707

Kuhnt, W., Holbourn, A., Schönfeld, J., Lindhorst, K., Gallagher, S., Keep, M., et al. (2017). *Cruise Report Sonne 257, WACHEIO—Western Australian Climate History from Eastern Indian Ocean Sediment Archives, Darwin—Fremantle, May 12, 2017 to June 04, 2017* (Vol. *260*). Institut Für Geowissenschaften, Christian-Albrechts-Universität Kiel. https://doi.org/10.2312/cr_so257

Kuhnt, W., Holbourn, A., Xu, J., Opdyke, B., De Deckker, P., Röhl, U., & Mudelsee, M. (2015). Southern Hemisphere control on Australian monsoon variability during the late deglaciation and Holocene. *Nature Communications*, *6*(5916), 1–7. https://doi.org/10.1038/ncomms6916

Laepple, T., Werner, M., & Lohmann, G. (2011). Synchronicity of Antarctic temperatures and local solar insolation on orbital timescales. *Nature*, *471*(7336), 91–94. https://doi.org/10.1038/nature09825

Lea, D. W., Pak, D. K., Belanger, C. L., Spero, H. J., Hall, M. A., & Shackleton, N. J. (2006). Paleoclimate history of Galápagos surface waters over the last 135,000 yr. *Quaternary Science Reviews*, *25*(11–12), 1152–1167. https://doi.org/10.1016/j.quascirev.2005.11.010

Lisiecki, L. E., & Raymo, M. E. (2005). A Pliocene-Pleistocene stack of 57 globally distributed benthic $\delta^{18}O$ records. *Paleoceanography*, *20*(1), 1–17. https://doi.org/10.1029/2004PA001071

Liu, J., Fu, G., Song, X., Charles, S. P., Zhang, Y., Han, D., & Wang, S. (2010). Stable isotopic compositions in Australian precipitation. *Journal of Geophysical Research Atmospheres*, *115*(23), 1–16. https://doi.org/10.1029/2010JD014403

Locarnini, R. A., Mishonov, A. V., Antonov, J. I., Boyer, T. P., Garcia, H. E., Baranova, O. K., et al. (2013). World Ocean Atlas 2013, Volume 1: Temperature. In S. Levitus, & A. Mishonov (Eds.), *NOAA Atlas NESDIS 73 National Oceanographic Data Center* (pp. 1–40). https://doi.org/10.7289/V55X26VD

Lowe, R. J., Ivey, G. N., Brinkman, R. M., & Jones, N. L. (2012). Seasonal circulation and temperature variability near the North West Cape of Australia. *Journal of Geophysical Research: Oceans*, *117*, C04010. https://doi.org/10.1029/2011JC007653

Lüthi, D., Le Floch, M., Bereiter, B., Blunier, T., Barnola, J. M., Siegenthaler, U., et al. (2008). High-resolution carbon dioxide concentration record 650,000–800,000 yr before present. *Nature*, *453*(7193), 379–382. https://doi.org/10.1038/nature06949

Mantsis, D. F., Lintner, B. R., Broccoli, A. J., Erb, M. P., Clement, A. C., & Park, H. S. (2014). The response of large-scale circulation to obliquity-induced changes in meridional heating gradients. *Journal of Climate*, *27*(14), 5504–5516. https://doi.org/10.1175/JCLI-D-13-00526.1

Martin, P. A., & Lea, D. W. (2002). A simple evaluation of cleaning procedures on fossil benthic foraminiferal Mg/Ca. *Geochemistry, Geophysics, Geosystems*, *3*(10), 1–8. https://doi.org/10.1029/2001GC000280

Matsumoto, K. (2007). Radiocarbon-based circulation age of the world oceans. *Journal of Geophysical Research*, *112*, C09004. https://doi.org/10.1029/2007JC004095

Medina-Elizalde, M., & Lea, D. W. (2005). The mid-Pleistocene transition in the tropical Pacific. *Science*, *310*(5750), 1009–1012. https://doi.org/10.1126/science.1115933

Milliman, J., & Farnsworth, K. (2011). Runoff, erosion, and delivery to the coastal ocean. In *River discharge to the coastal ocean: A global synthesis* (pp. 13–39). Cambridge University Press. https://doi.org/10.1017/cbo9780511781247.003

Mohtadi, M., Oppo, D. W., Steinke, S., Stuut, J. B. W., De Pol-Holz, R., Hebbeln, D., & Lückge, A. (2011). Glacial to Holocene swings of the Australian-Indonesian monsoon. *Nature Geoscience*, *4*(8), 540–544. https://doi.org/10.1038/ngeo1209

Mohtadi, M., Prange, M., Oppo, D. W., De Pol-Holz, R., Merkel, U., Zhang, X., et al. (2014). North Atlantic forcing of tropical Indian Ocean climate. *Nature*, *509*(7498), 76–80. https://doi.org/10.1038/nature13196

Morimoto, M., Abe, O., Kayanne, H., Kurita, N., Matsumoto, E., & Yoshida, N. (2002). Salinity records for the 1997–98 El Niño from Western Pacific corals. *Geophysical Research Letters*, *29*(11), 351–354. https://doi.org/10.1029/2001GL013521

Muller, J., Kylander, M., Wüst, R. A. J., Weiss, D., Martinez-Cortizas, A., LeGrande, A. N., et al. (2008). Possible evidence for wet Heinrich phases in tropical NE Australia: The Lynch's Crater deposit. *Quaternary Science Reviews*, *27*(5–6), 468–475. https://doi.org/10.1016/j.quascirev.2007.11.006

Muller, J., McManus, J. F., Oppo, D. W., & Francois, R. (2012). Strengthening of the Northeast Monsoon over the Flores Sea, Indonesia, at the time of Heinrich event 1. *Geology*, *40*(7), 635–638. https://doi.org/10.1130/G32878.1

Pattiaratchi, C. (2006). Surface and sub-surface circulation and water masses off Western Australia. *Bulletin of the Australian Meteorological and Oceanographic Society*, *19*(5), 95–104.

Pei, R., Kuhnt, W., Holbourn, A., Hingst, J., Koppe, M., Schultz, J., et al. (2021). Monitoring Australian monsoon variability over the past four glacial cycles. *Palaeogeography, Palaeoclimatology, Palaeoecology*, *568*, 110280. https://doi.org/10.1016/j.palaeo.2021.110280

Phillips, H. E., Wijffels, S. E., & Feng, M. (2005). Interannual variability in the freshwater content of the Indonesian-Australian Basin. *Geophysical Research Letters*, *32*(3), 1–5. https://doi.org/10.1029/2004GL021755

Ridgway, K. R., & Condie, S. A. (2004). The 5,500 km-long boundary flow off western and southern Australia. *Journal of Geophysical Research: Oceans*, *109*(C4), 1–18. https://doi.org/10.1029/2003JC001921

Ridgway, K. R., & Godfrey, J. S. (2015). The source of the Leeuwin Current seasonality. *Journal of Geophysical Research: Oceans*, *120*(10), 6843–6864. https://doi.org/10.1002/2015JC011049

Rosenthal, Y., Holbourn, A. E., Kulhanek, D. K., & the Exp. 363 Scientists. (2018). Western Pacific Warm Pool. In *Proceedings of the International Ocean Discovery Program* (Vol. *363*). International Ocean Discovery Program. https://doi.org/10.14379/iodp.proc.363.2018

Rossignol-Strick, M. (1983). African monsoons, an immediate climate response to orbital insolation. *Nature*, *304*(5921), 46–49. https://doi.org/10.1038/304046a0

Sarnthein, M., Grootes, P. M., Holbourn, A., Kuhnt, W., & Kühn, H. (2011). Tropical warming in the Timor Sea led deglacial Antarctic warming and atmospheric CO_2 rise by more than 500 yr. *Earth and Planetary Science Letters*, *302*(3–4), 337–348. https://doi.org/10.1016/j.epsl.2010.12.021

Schlitzer, R. (2021). *Ocean Data View*. Retrieved from odv.awi.de

Schröder, J. F., Holbourn, A., Kuhnt, W., & Küssner, K. (2016). Variations in sea surface hydrology in the southern Makassar Strait over the past 26 kyr. *Quaternary Science Reviews*, *154*, 143–156. https://doi.org/10.1016/j.quascirev.2016.10.018

Schröder, J. F., Kuhnt, W., Holbourn, A., Beil, S., Zhang, P., Hendrizan, M., & Xu, J. (2018). Deglacial warming and hydroclimate variability in the Central Indonesian Archipelago. *Paleoceanography and Paleoclimatology*, *33*(9), 974–993. https://doi.org/10.1029/2018PA003323

Shakun, J. D., Clark, P. U., He, F., Marcott, S. A., Mix, A. C., Liu, Z., et al. (2012). Global warming preceded by increasing carbon dioxide concentrations during the last deglaciation. *Nature*, *484*(7392), 49–54. https://doi.org/10.1038/nature10915

Smith, R. L., Huyer, A., Godfrey, J. S., & Church, J. A. (1991). The Leeuwin Current off Western Australia, 1986–1987. *Journal of Physical Oceanography*, *21*(2), 323–345. https://doi.org/10.1175/1520-0485(1991)021<0323:TLCOWA>2.0.CO;2

Spooner, M. I., De Deckker, P., Barrows, T. T., & Fifield, L. K. (2011). The behavior of the Leeuwin Current offshore NW Australia during the last five glacial-interglacial cycles. *Global and Planetary Change*, *75*(3–4), 119–132. https://doi.org/10.1016/j.gloplacha.2010.10.015

Stager, J. C., Ryves, D. B., Chase, B. M., & Pausata, F. S. R. (2011). Catastrophic drought in the Afro-Asian monsoon region during Heinrich event 1. *Science*, *331*(6022), 1299–1302. https://doi.org/10.1126/science.1198322

Stott, L., Timmermann, A., & Thunell, R. (2007). Southern Hemisphere and deep-sea warming led deglacial atmospheric CO_2 rise and tropical warming. *Science*, *318*(5849), 435–438. https://doi.org/10.1126/science.1143791

Taylor, J. G., & Pearce, A. F. (1999). Ningaloo Reef currents: Implications for coral spawn dispersal, zooplankton, and whale shark abundance. *Journal of the Royal Society of Western Australia*, *82*, 57–65.

Thompson, A. F., & Richards, K. J. (2011). Low frequency variability of Southern Ocean jets. *Journal of Geophysical Research*, *116*(C9), 1–17. https://doi.org/10.1029/2010JC006749

Timmermann, A., Timm, O., Stott, L., & Menviel, L. (2009). The roles of CO_2 and orbital forcing in driving Southern Hemispheric temperature variations during the last 21,000 yr. *Journal of Climate*, *22*(7), 1626–1640. https://doi.org/10.1175/2008JCLI2161.1

Uemura, R., Motoyama, H., Masson-Delmotte, V., Jouzel, J., Kawamura, K., Goto-Azuma, K., et al. (2018). Asynchrony between Antarctic temperature and CO_2 associated with obliquity over the past 720,000 yr. *Nature Communications*, *9*(1), 1–11. https://doi.org/10.1038/s41467-018-03328-3

Waelbroeck, C., Labeyrie, L., Michel, E., Duplessy, J. C., McManus, J. F., Lambeck, K., et al. (2002). Sea-level and deep water temperature changes derived from benthic foraminifera isotopic records. *Quaternary Science Reviews*, *21*(1–3), 295–305. https://doi.org/10.1016/S0277-3791(01)00101-9

Weller, E., Holliday, D., Feng, M., Beckley, L., & Thompson, P. (2011). A continental shelf scale examination of the Leeuwin Current off Western Australia during the austral autumn-winter. *Continental Shelf Research*, *31*(17), 1858–1868. https://doi.org/10.1016/j.csr.2011.08.008

Woo, M., Pattiaratchi, C., & Schroeder, W. (2006). Dynamics of the Ningaloo Current off Point Cloates, Western Australia. *Marine and Freshwater Research*, *57*, 291–301. https://doi.org/10.1071/MF05106

Xu, J., Holbourn, A., Kuhnt, W., Jian, Z., & Kawamura, H. (2008). Changes in the thermocline structure of the Indonesian outflow during Terminations I and II. *Earth and Planetary Science Letters*, *273*(1–2), 152–162. https://doi.org/10.1016/j.epsl.2008.06.029

Xu, J., Kuhnt, W., Holbourn, A., Andersen, N., & Bartoli, G. (2006). Changes in the vertical profile of Indonesian Throughflow during Termination II: Evidence from the Timor Sea. *Paleoceanography*, *21*(4), 1–14. https://doi.org/10.1029/2006PA001278

Xu, J., Kuhnt, W., Holbourn, A., Regenberg, M., & Andersen, N. (2010). Indo-Pacific warm pool variability during the Holocene and last glacial maximum. *Paleoceanography*, *25*(4). https://doi.org/10.1029/2010PA001934

Zhang, N., Feng, M., Du, Y., Lan, J., & Wijffels, S. E. (2016). Seasonal and interannual variations of mixed layer salinity in the southeast tropical Indian Ocean. *Journal of Geophysical Research: Oceans*, *121*(7), 4716–4731. https://doi.org/10.1002/2016JC011854

Zhang, P., Xu, J., Holbourn, A., Kuhnt, W., Beil, S., Li, T., et al. (2020). Indo-Pacific hydroclimate in response to changes of the Intertropical Convergence Zone: Discrepancy on precession and obliquity bands over the last 410 kyr. *Journal of Geophysical Research: Atmospheres*, *125*(14), 1–10. https://doi.org/10.1029/2019JD032125

Zweng, M. M., Reagan, J. R., Antonov, J. I., Locarnini, R. A., Mishonov, A. V., Boyer, T. P., et al. (2013). World Ocean Atlas 2013, Volume 2: Salinity. In S. Levitus, & A. Mishonov (Eds.), *NOAA Atlas NESDIS* (Vol. *74*, pp. 1–39). National Oceanographic Data Center. Retrieved from https://www.ncei.noaa.gov/data/oceans/woa/WOA13/DOC/woa13_vol2.pdf